

Large thermo-spin effects in Heusler alloy based spin-gapless semiconductor thin films

Amit Chanda^{1*}, Deepika Rani², Derick DeTellem¹, Noha Alzahrani¹, Dario A. Arena¹, Sarath Witanachchi¹, Ratnamala Chatterjee², Manh-Huong Phan¹ and Hariharan Srikanth^{1*}

¹ Department of Physics, University of South Florida, Tampa FL 33620

² Physics Department, Indian Institute of Technology Delhi, New Delhi - 110016

*Corresponding authors: achanda@usf.edu; sharihar@usf.edu

Keywords: Longitudinal spin Seebeck effect, Anomalous Nernst effect, Spin gapless semiconductor, Heusler alloy, Magnetic anisotropy, Gilbert damping

Abstract

Recently, Heusler alloys-based spin gapless semiconductors (SGSs) with high Curie temperature (T_C) and sizeable spin polarization have emerged as potential candidates for tunable spintronic applications. We report comprehensive investigation of the temperature dependent ANE and intrinsic longitudinal spin Seebeck effect (LSSE) in CoFeCrGa thin films grown on MgO substrates. Our findings show the anomalous Nernst coefficient for the MgO/CoFeCrGa (95 nm) film is $\approx 1.86 \mu\text{V} \cdot \text{K}^{-1}$ at room temperature which is nearly two orders of magnitude higher than that of the bulk polycrystalline sample of CoFeCrGa ($\approx 0.018 \mu\text{V} \cdot \text{K}^{-1}$) but comparable to that of the magnetic Weyl semimetal Co_2MnGa thin film ($\approx 2 - 3 \mu\text{V} \cdot \text{K}^{-1}$). Furthermore, the LSSE coefficient for our MgO/CoFeCrGa(95nm)/Pt(5nm) heterostructure is $\approx 20.5 \text{ nV} \cdot \text{K}^{-1} \cdot \Omega^{-1}$ at room temperature which is twice larger than that of the half-metallic ferromagnetic $\text{La}_{0.7}\text{Sr}_{0.3}\text{MnO}_3$ thin films ($\approx 9 \text{ nV} \cdot \text{K}^{-1} \cdot \Omega^{-1}$). We show that both ANE and LSSE coefficients follow identical temperature dependences and exhibit a

maximum at ≈ 225 K which is understood as the combined effects of inelastic magnon scatterings and reduced magnon population at low temperatures. Our analyses not only indicate that the extrinsic skew scattering is the dominating mechanism for ANE in these films but also provide critical insights into the functional form of the observed temperature dependent LSSE at low temperatures. Furthermore, by employing radio frequency transverse susceptibility and broadband ferromagnetic resonance in combination with the LSSE measurements, we establish a correlation among the observed LSSE signal, magnetic anisotropy and Gilbert damping of the CoFeCrGa thin films, which will be beneficial for fabricating tunable and highly efficient Heusler alloys based spin caloritronic nanodevices.

1. INTRODUCTION

The past few years have witnessed extensive research efforts in the field of spin caloritronics for the development of highly efficient next-generation spin-based electronic devices by combining the versatile advantages of spintronics and thermoelectricity, with the aim of finding novel avenues for waste heat recovery and thermoelectric energy conversion^{1,2}. Fundamental knowledge of the interplay between heat, charge, and spin degrees of freedom not only allowed us to understand how thermal gradients can be utilized to manipulate and control the flow of spin angular momenta inside a material at nanoscale, but also helped the scientific community to explore various intriguing thermo-spin transport phenomena, such as the anomalous Nernst effect (ANE)³, spin Nernst effect⁴, spin Seebeck effect^{5,6}, spin Peltier effect⁷ and so on.

The ANE refers to the generation of a transverse thermoelectric voltage in a magnetic conductor/semiconductor by the application of a thermal gradient and an external magnetic field^{8,9}. The ANE has been observed in a large range of magnetic materials, from half-metallic ferromagnets such as hole-doped manganites¹⁰, cobaltites¹¹⁻¹³, spin gapless semiconductors¹⁴ to ferrimagnets such as iron oxide¹⁵, Mn-based nitride¹⁶, as well as unconventional magnetic systems with topologically non-trivial phases such as topological full Heusler ferromagnets^{3,17-19}, ferromagnetic Weyl semimetals^{20,21}, two-dimensional topological van der Waals ferromagnets^{22,23}, chiral⁸ and canted²⁴ topological antiferromagnets *etc.* In a topological magnetic material, charge carriers moving through a periodic potential with strong spin-orbit coupling (SOC) acquire an additional anomalous velocity perpendicular to their original trajectory due to the non-zero Berry curvature at the Fermi level²⁵. This anomalous velocity causes a real space spin selective deflection of the charge carriers and leads to a potentially large ANE response in these topological magnetic materials compared to conventional magnets²⁵. In addition to the aforementioned intrinsic origin, ANE can also originate from extrinsic

effects for example, asymmetric skew scattering of charge carriers as observed in Heusler ferromagnets^{14,26,27}, hole-doped manganites¹⁰, cobaltites¹¹⁻¹³, spin gapless semiconductors¹⁴, iron oxide¹⁵ etc.

On the other hand, the longitudinal spin Seebeck effect (LSSE) refers to the thermal generation of magnonic spin current in a ferromagnetic (FM) material by the concurrent applications of a temperature gradient and an external magnetic field across a FM/heavy metal (HM) bilayer structure and injection of that spin current to the adjacent HM layer with strong SOC, which is then converted into electrically detectable charge current in the HM layer via the inverse spin Hall effect (ISHE)^{1,28-30}. The bilayer structure consisting of the ferrimagnetic insulator $\text{Y}_3\text{Fe}_5\text{O}_{12}$ (YIG) and Pt is known as the benchmark system for generating pure spin current and hence, LSSE^{28,30-34}. Apart from YIG, other magnetic insulators for example, the compensated ferrimagnetic insulator $\text{Gd}_3\text{Fe}_5\text{O}_{12}$,^{35,36} insulating spinel ferrites CoFe_2O_4 , NiFe_2O_4 ^{37,38}, noncollinear antiferromagnetic insulator LuFeO_3 ³⁹ etc., have also emerged as promising spin caloritronic materials. Nevertheless, observation of LSSE is not only restricted to magnetic insulators, but it has also been observed in metallic^{5,40}, half-metallic⁴¹⁻⁴³ and semiconducting ferromagnets⁴⁴.

Although ANE and LSSE are two distinct types of magnetothermoelectric phenomena, they share common origin for materials exhibiting extrinsic effects dominated ANE⁴⁵. In both the cases, simultaneous application of thermal gradient and external magnetic field generates magnonic excitations. While in the case of ANE, the thermally generated magnons transfer spin angular momenta to the itinerant electrons of the FM via the electron-magnon scattering and thereby dynamically spin polarizes them, in the case of LSSE, a spatial gradient of those thermally generated magnons leads to magnon accumulation close to the FM/HM interface and

pumps spin current to the HM layer⁴⁵. Large magnon-induced ANE has been observed in MnBi single crystal⁴⁵. However, observation of large ANE in a FM conductor does not necessarily indicate a promise for a large LSSE, and vice versa. Therefore, it would be technologically advantageous from the perspective of spin caloritronic device applications and thermal energy harnessing to search for a FM material that can simultaneously exhibit large LSSE and ANE.

In recent years, Heusler alloys-based spin gapless semiconductors (SGSs) have emerged as promising magnetic materials for tunable spintronic applications as they not only combine the characteristics of both half-metallic ferromagnets and gapless semiconductors,⁴⁶ but also possess high Curie temperature (T_C) and substantial spin polarization⁴⁷⁻⁵⁰. We have recently observed large ANE in the bulk sample of Heusler alloy based SGS: CoFeCrGa with $T_C \approx 690$ K,^{14,50,51} which was the first experimental observation of ANE in the SGS family. Our fascinating observation motivated us to explore ANE as well as LSSE in the CoFeCrGa thin films. Although SGS has been theoretically predicted to be a promising candidate for spintronic applications⁵², there is no previous experimental study on the thermo-spin transport phenomena, especially LSSE in SGS thin films. In this paper, we report on the temperature dependent ANE and LSSE in the CoFeCrGa single layer and CoFeCrGa/Pt bilayer films with different CoFeCrGa film thicknesses. We found that both ANE and LSSE coefficients follow identical temperature dependences and exhibit a maximum at ≈ 225 K which is understood as the combined effects of inelastic magnon scatterings and reduced magnon population at low temperatures. Our analyses not only indicate that the extrinsic skew scattering is the dominating mechanism for ANE in these films but also provide critical insights into the functional form of the observed temperature dependent LSSE. Furthermore, we have established a correlation among the observed LSSE signal, magnetic anisotropy and Gilbert damping of the CoFeCrGa thin films which will be beneficial for fabricating tunable and efficient spin caloritronic devices.

2. EXPERIMENTAL SECTION

The thin films of CoFeCrGa were grown on single crystal MgO (001) substrates of surface area $5 \times 5 \text{ mm}^2$ using an excimer KrF pulsed laser deposition (PLD) system. The films were deposited at $500 \text{ }^\circ\text{C}$ and were further annealed in-situ at $500 \text{ }^\circ\text{C}$ for 30 min to further enhance the chemical order and crystallization. The film surface morphology was investigated by field emission gun – scanning electron microscopy (FEG-SEM) and atomic force microscopy (AFM), while the structural properties of the thin films were identified by x-ray diffraction (XRD) using monochromatic Cu $K\alpha$ radiation.

AFM and temperature dependent magnetic force microscopy (MFM) measurements were performed on a Hitachi 5300E system. All measurements were done under high vacuum ($P \leq 10^{-6}$ Torr). MFM measurements utilized PPP-MFMR tips, which were magnetized out-of-plane with respect to the tip surface via a permanent magnet. Films were first magnetized to their saturation magnetization by being placed in a 1T static magnetic field, in-plane with the film surface. After that AC demagnetization of the film was implemented before initiating the MFM scans. After scans were performed, first a linear background was subtracted which comes from the film not being completely flat on the sample stage. After that, a parabolic background was subtracted, which arises from the nonlinear motion of the piezoelectric crystal that drives the x - y translation. Phase standard deviation was determined by fitting a Gaussian to the image phase distribution and extracting the standard deviation from the fit parameters.

The DC magnetic measurements on the samples at temperatures between 100 K and 300 K were performed using a vibrating sample magnetometer (VSM) attached to a physical property measurement system (PPMS), Quantum Design. A linear background originating from the diamagnetic MgO substrate was thereby subtracted. Due to a trapped remanent field

inside the superconducting coils, the measured magnetic field was corrected using a paramagnetic reference sample.

The longitudinal electrical resistivity, longitudinal Seebeck coefficient, and thermal conductivity of the bulk samples were simultaneously measured with the thermal transport option (TTO) of the PPMS. The electrical resistivity and Hall measurements on the thin film samples were performed using the DC resistivity option of the PPMS by employing a standard four point measurement technique with sourcing currents of 500 μA and 1 mA, respectively.

The temperature dependence of the effective magnetic anisotropy fields of the MgO/CoFeCrGa films were measured by using a radio frequency (RF) transverse susceptibility (TS) measurement technique that exploits a self-resonant tunnel diode oscillator (TDO) circuit with a resonance frequency of ≈ 12 MHz^{53,54}. The PPMS was used as a platform to sweep the external DC magnetic field and temperature. During the TS measurement, the MgO/CoFeCrGa thin film samples were firmly placed inside an inductor coil (L), which is a component of an LC resonator circuit. The coil containing the sample was positioned at the base of the PPMS sample chamber through a multifunctional PPMS probe in such a way that the axial RF magnetic field generated inside the coil stayed parallel to the film surface, but perpendicular to the DC magnetic field generated by the superconducting magnet of the PPMS. In presence of both the RF and DC magnetic fields, the dynamic transverse susceptibility of the sample changes which eventually changes the resonance frequency of the LC circuit⁵³. From the magnetic field dependence of the shift in the resonance frequency recorded by an Agilent frequency counter, we obtained the field dependent transverse susceptibility.

The ANE and LSSE measurements were performed using a custom-designed setup assembled on a universal PPMS sample puck, as shown in our previous reports^{14,36}. For both the measurements, the thin film samples were sandwiched between two copper plates. A single layer of thin Kapton tape was thermally anchored to the bare surfaces of the top (cold) and bottom (hot) copper plates. Cryogenic Apiezon N-grease was used to create good thermal connectivity between the thin film surface and that of the Kapton tapes. A resistive heater (PT-100 RTD sensor) and a calibrated Si-diode thermometer (DT-621-HR silicon diode sensor) were attached to each of those copper plates. The temperatures of both these copper plates were monitored and controlled individually by employing two distinct separate temperature controllers (Scientific Instruments Model no. 9700). The top copper plate was thermally linked to the base of the PPMS universal puck using a pair of molybdenum screws and a 4 mm thick Teflon block was thermally sandwiched between the universal PPMS puck base and the bottom copper plate to maintain a temperature difference of ~ 10 K between the hot copper plate and the PPMS universal puck base. The Ohmic contacts for the ANE and LSSE voltage measurements were made by using a pair of thin gold wires of 25 μm diameter to the Pt layer by high quality conducting silver paint (SPI Supplies). In presence of an applied temperature gradient along the z -direction, and an in-plane external DC magnetic field applied along the x -direction, the transverse thermoelectric voltage generated along the y -direction across the Pt layer due to the ISHE (V_{ISHE}) and across the CoFeCrGa film itself due to the ANE was recorded with a Keithley 2182a nanovoltmeter.

Broadband ferromagnetic resonance (FMR) measurements were performed using a broadband FMR spectrometer (NanOscTM Phase-FMR, Quantum Design Inc., USA) integrated to the Dynacool PPMS⁵⁵.

3. RESULTS AND DISCUSSION

3.1. Structural and morphological properties

Figure 1(a) shows the X-ray 2θ - ω (out of plane) diffraction pattern for CoFeCrGa (95nm) film grown on MgO (001) substrate. In addition to the peaks corresponding to the MgO substrate, there are additional (002) and (004) diffraction peaks from the film, indicating the growth in the (001) orientation. The formation of B2 CoFeCrGa structure is confirmed by the presence of (002) peak. To find the CoFeCrGa (220) peak intensity, a 2θ - θ scan was performed with $\chi=45^\circ$ as shown in **Fig. 1**(b). The lattice parameter as estimated by applying the Bragg equation to the (022) peak, was found to be 5.76 Å.

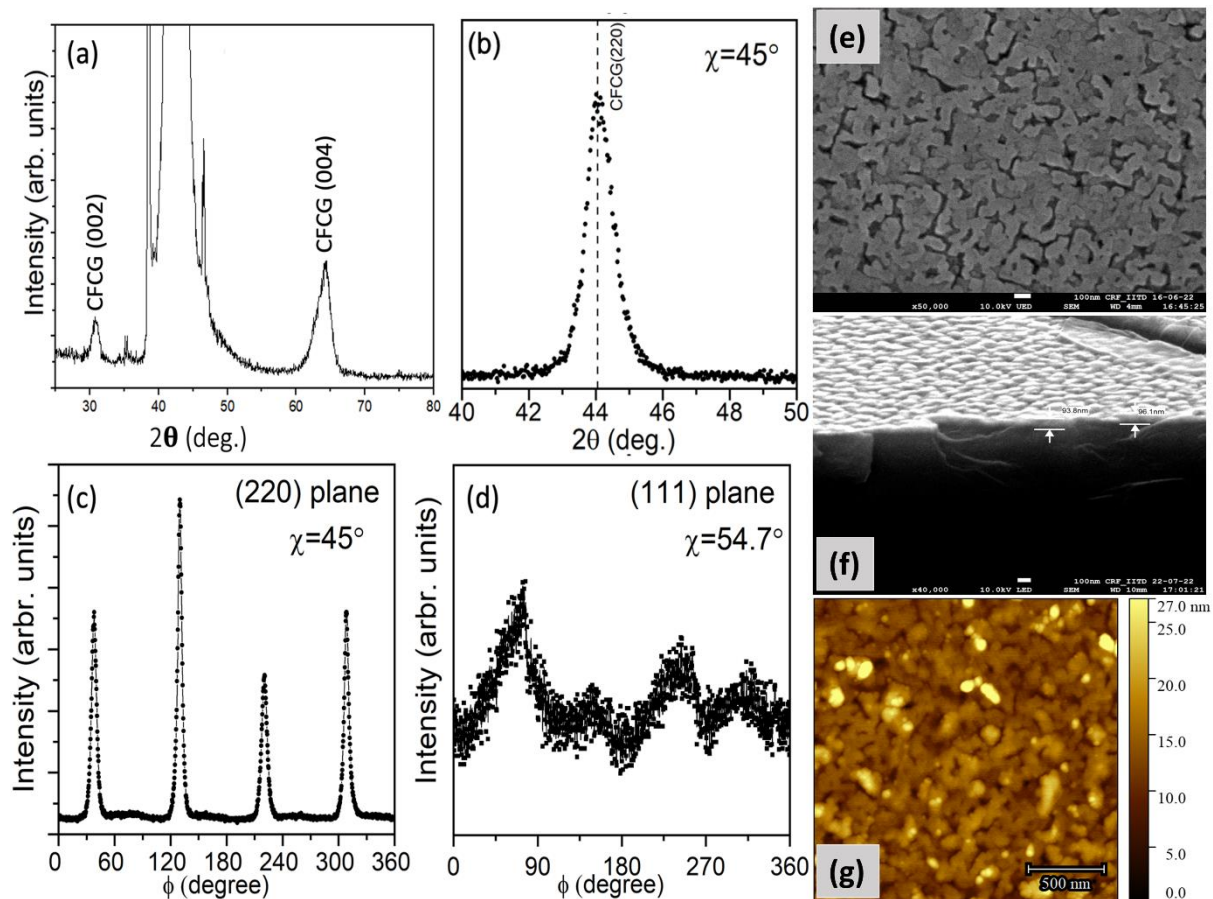


Figure 1. (a) XRD of MgO/CoFeCrGa(95nm) film: ω - 2θ (out-of-plane) scan. (b) The 2θ - θ scan of the (022) plane. (c) Phi-scan of the (022) plane. (d) ϕ -scan of the (111) plane. (e) FEG-SEM, (f) Cross sectional SEM image and (g) AFM image for the MgO/CoFeCrGa(95nm) film.

To further confirm the epitaxial growth of the CoFeCrGa (95nm) film, ϕ -scan was performed for the (220) and (111) planes by tilting the sample, i.e., $\chi = 45^\circ$ for the (220) plane and $\chi = 54.7^\circ$ for the (111) plane (**Fig. 1(c)**, and **Fig. 1(d)**). The ϕ - scans of both (220) and (111) plane show a four-fold symmetry, as four well defined peaks periodically separated from each other by 90° were observed. The presence of both (111) and (200) peaks rule out the possibility of complete A2 or B2 disorder, however partial disorder can still be present. The chemical composition was interpreted by the scanning electron microscopy energy-dispersive spectroscopy (SEM-EDS) measurements and was found to be $\text{Co}_{1.05}\text{Fe}_{1.05}\text{Cr}_{0.9}\text{Ga}_{0.99}$, which is very close to the ideal stoichiometric composition expected for an equiatomic quaternary Heusler alloy. The surface morphology of the film obtained from the FEG-SEM image is shown in **Fig. 1(e)**, which indicates that the film is homogenous, which was further confirmed by AFM measurements as shown in **Fig. 1(g)**. A low root-mean-square (RMS) roughness of ≈ 2.5 nm is achieved for the CoFeCrGa film, as noticeable in the AFM image shown in **Fig. 1(g)**. The cross-section SEM image of the film is shown in **Fig. 1(f)**, which indicates that the film thickness ($\sim 95 \pm 5$ nm).

In **Fig. 2**, we show the temperature dependent magnetic force microscopy (MFM) images recorded on the MgO/CoFeCrGa(95nm) film. The MFM image at 300 K (see **Fig. 2(a)**) shows a bright/dark contrast with highly irregular shaped features indicating cloudlike domain-clusters⁵⁶. Note that in MFM, the domain-image contrast is determined by the magnetic force-gradient $\left(\frac{dF}{dz}\right)$ between the sample and the MFM tip (magnetized \perp to the film-surface), which is proportional to the perpendicular component of the stray field of the film^{57,58}. For our film, due to low bright/dark contrast patterns of the MFM images in the T -range: $160\text{K} \leq T \leq 300$ K (**Fig. 2(a)-(e)**), the domain boundaries are not as well-defined as observed in films with strong PMA⁵⁹.

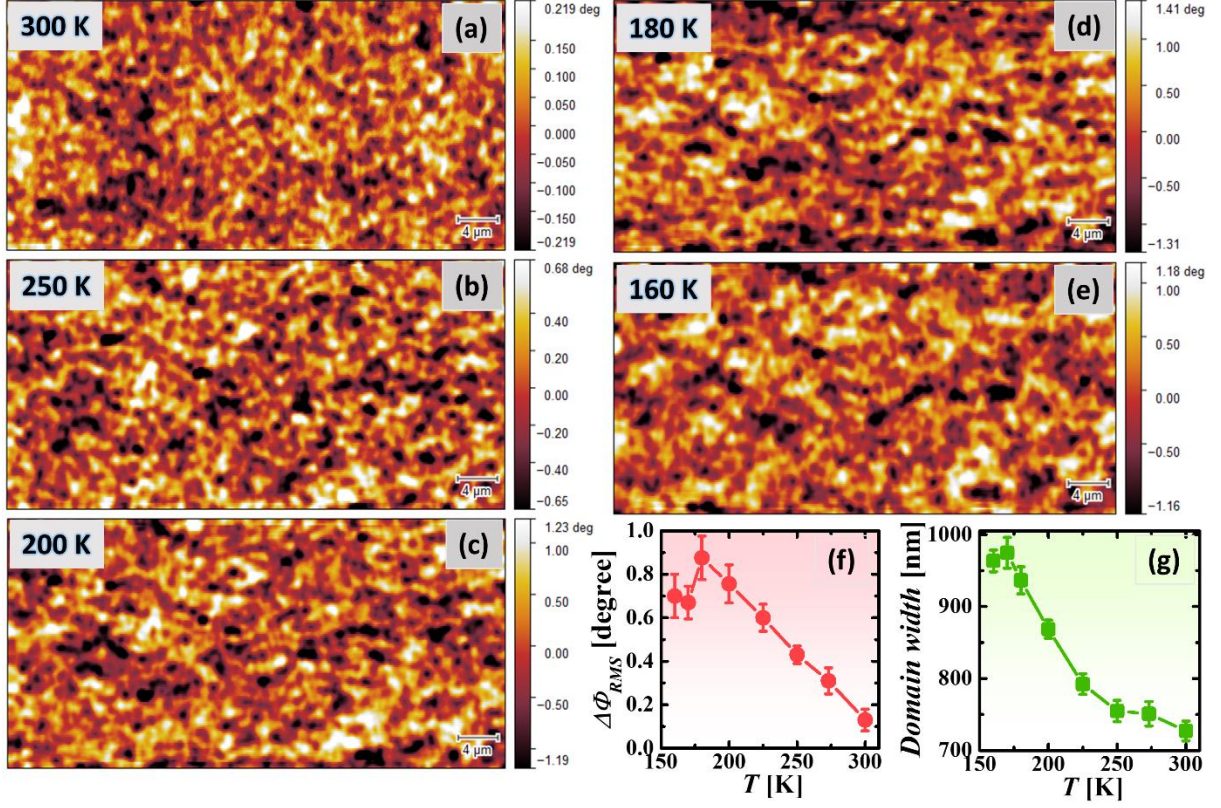


Figure 2. Magnetic force microscopy (MFM) images of MgO/CoFeCrGa(95nm) film measured at (a) $T = 300$ K, (b) $T = 250$ K, (c) $T = 200$ K, (d) $T = 180$ K, and (e) $T = 160$ K while cooling the sample after applying an IP magnetic field (higher than the IP saturation field) and then AC demagnetization of the sample at 300 K. (f) The RMS value of the phase shift, $\Delta\phi_{RMS}$ as a function of temperature for the MgO/CoFeCrGa(95nm) film extracted from the MFM images. (g) The average domain width as a function of temperature obtained from the MFM images.

A steep increase in the root mean square (RMS) value of the phase shift,⁵⁷ $\Delta\phi_{RMS} \approx \frac{Q}{K} \left[\frac{dF}{dz} \right]$ (Q = quality factor and K = spring constant of the tip; hence, $\Delta\phi_{RMS} \propto$ average domain contrast⁵⁸) has also been observed below 300 K (see Fig. 2(f)). However, $\Delta\phi_{RMS}$ decreases slightly below 180 K. Average domain widths were determined by calculating the 2D autocorrelation across the MFM images, then determining the full-width half-max (FWHM) of arbitrary lines through the 2D autocorrelation spectra. As shown in Fig. 2(g), the average domain width also increases with decreasing temperature followed by a slight decrease below 170 K.

3.2. Magnetic and electrical transport properties

Previous studies on bulk CoFeCrGa^{50,51} as well as MgO/CoFeCrGa thin films⁶⁰ reveal that the ferromagnetic transition temperature of this sample is very high (at least ≥ 500 K). The main panel of Fig. 3(a) shows the magnetic field dependence of magnetization, $M(H)$ of our MgO/CoFeCrGa film measured at selected temperatures in the range: $125 \text{ K} \leq T \leq 300 \text{ K}$ in presence of an in-plane sweeping magnetic field. The $M(H)$ loops exhibit very small coercivity throughout the measured temperature range.

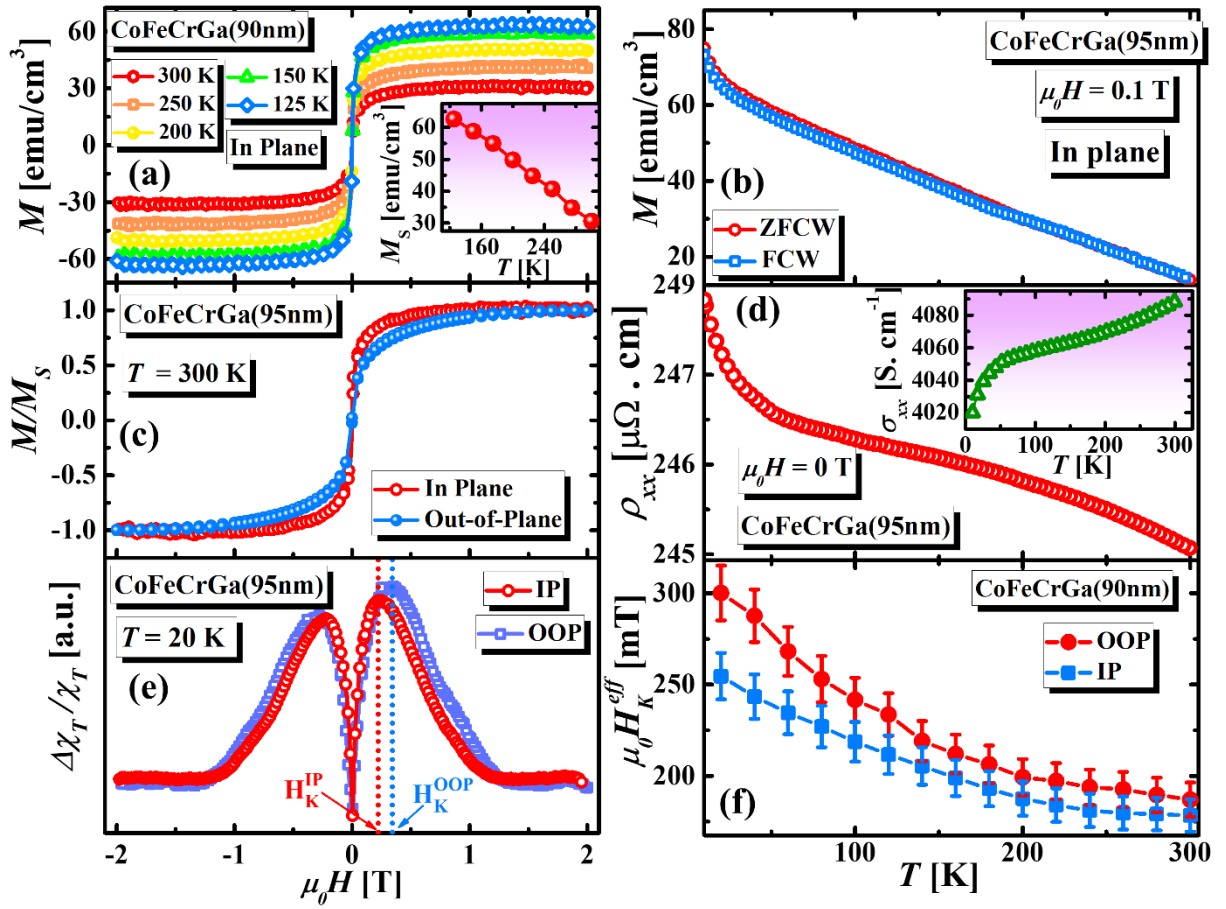


Figure 3. (a) Main panel: magnetic field dependence of magnetization, $M(H)$ of our MgO/CoFeCrGa(95nm) film measured at selected temperatures in the range: $125 \text{ K} \leq T \leq 300 \text{ K}$ in presence of an in-plane sweeping magnetic field, inset: temperature dependence of the saturation magnetization, M_S . (b) Temperature dependence of magnetization, $M(T)$ measured in zero-field-cooled warming (ZFCW) and field-cooled-warming (FCW) protocols in presence of an external magnetic field: $\mu_0 H = 0.1 \text{ T}$. (c) Normalized $M(H)$ hysteresis loops at $T = 300 \text{ K}$ for the in-plane (IP) and out-of-plane (OOP) configurations. (d) Main panel: temperature dependence of magnetization, $M(T)$ measured in zero-field-cooled warming (ZFCW) and field-cooled-warming (FCW) protocols in presence of an external magnetic field: $\mu_0 H = 0.1 \text{ T}$. (e) Normalized $M(H)$ hysteresis loops at $T = 300 \text{ K}$ for the in-plane (IP) and out-of-plane (OOP) configurations. (f) Temperature dependence of magnetization, $M(T)$ measured in zero-field-cooled warming (ZFCW) and field-cooled-warming (FCW) protocols in presence of an external magnetic field: $\mu_0 H = 0.1 \text{ T}$.

temperature dependence of longitudinal resistivity, $\rho_{xx}(T)$ for the MgO/CoFeCrGa film in the temperature range: $10 \text{ K} \leq T \leq 300 \text{ K}$, inset shows corresponding temperature dependence of electrical conductivity, $\sigma_{xx}(T)$. (e) The bipolar field scans ($+H_{DC}^{max} \rightarrow -H_{DC}^{max} \rightarrow +H_{DC}^{max}$) of $\frac{\Delta\chi_T}{\chi_T}(H_{DC})$ for MgO/CoFeCrGa(95nm) film measured at $T = 20 \text{ K}$ for both IP (H_{DC} is parallel to the film surface) and OOP (H_{DC} is perpendicular to the film surface) configurations. (f) Temperature variations of the effective anisotropy fields: H_K^{IP} and H_K^{OOP} for our MgO/CoFeCrGa(95nm) film.

As shown in the inset of **Fig. 3(a)**, the saturation magnetization, M_S increases almost linearly with decreasing temperature, which is in agreement with the temperature dependent $\Delta\phi_{RMS}$ obtained from the MFM images⁵⁸. In **Fig. 3(b)**, we show the temperature dependence of magnetization, $M(T)$ measured in zero-field-cooled warming (ZFCW) and field-cooled-warming (FCW) protocols in presence of an external magnetic field: $\mu_0 H = 0.1 \text{ T}$. It is evident that both ZFCW and FCW $M(T)$ increases with decreasing temperature down to 10 K below which it shows a slight up-turn. Furthermore, the ZFCW and FCW $M(T)$ curves do not exhibit any considerable bifurcation at low temperatures which is indicative of the absence of any glassy magnetic ground state. **Fig. 3(c)** shows the normalized $M(H)$ hysteresis loops at $T = 300 \text{ K}$ for the in-plane (IP) and out-of-plane (OOP) configurations confirming the soft ferromagnetic nature of the film along the IP direction, which is consistent with a recent report on this system⁶⁰.

The main panel of **Fig. 3(d)** demonstrates the T -dependence of longitudinal resistivity, $\rho_{xx}(T)$ for the MgO/CoFeCrGa film in the temperature range: $10 \text{ K} \leq T \leq 300 \text{ K}$. It is obvious that $\rho_{xx}(T)$ exhibits semiconducting-like resistivity ($\frac{\partial\rho_{xx}}{\partial T} > 0$) throughout the temperature range. The inset of **Fig. 3(d)** shows the T -dependence of electrical conductivity, $\sigma_{xx}(T)$ for the MgO/CoFeCrGa film. Note that the values of both $\rho_{xx}(T)$ and $\sigma_{xx}(T)$ for our MgO/CoFeCrGa film are quite close to those reported on the same film with 12 nm thickness⁶⁰.

Furthermore, the linear temperature coefficient of the resistivity for our MgO/CoFeCrGa film was found to be $\approx -1.37 \times 10^{-10} \Omega \text{ m/K}$, which is of the same magnitude to that reported for different Heusler alloys-based spin gapless semiconductors (SGSs), such as Mn_2CoAl ($-1.4 \times 10^{-9} \Omega \text{ m/K}$),⁴⁷ CoFeMnSi ($-7 \times 10^{-10} \Omega \text{ m/K}$),⁶¹ CoFeCrAl ($-5 \times 10^{-9} \Omega \text{ m/K}$),⁶² and CoFeCrGa ($-1.9 \times 10^{-9} \Omega \text{ m/K}$)⁶⁰ thin films.

We have also performed radio frequency (RF) transverse susceptibility (TS) measurements on our MgO/CoFeCrGa film in the temperature range: $20 \text{ K} \leq T \leq 300 \text{ K}$ to determine the temperature evolution of effective magnetic anisotropy. This technique can accurately determine the dynamical magnetic response of a magnetic material in presence of a DC magnetic field (H_{DC}) and a transverse RF magnetic field (H_{RF}) with small and fixed amplitude.⁶³ When H_{DC} is scanned from positive to negative saturations, the TS of a magnetic material with uniaxial anisotropy demonstrates well-defined peaks at the anisotropy fields, $H_{DC} = \pm H_K$.⁶⁴ But for a magnetic material comprising of randomly dispersed magnetic easy axes, the TS shows broad maxima at the effective anisotropy fields, $H_{DC} = \pm H_K^{eff}$. Here, we show the TS spectra as percentage change of the measured transverse susceptibility as, $\frac{\Delta\chi_T}{\chi_T}(H_{DC}) = \frac{\chi_T(H_{DC}) - \chi_T(H_{DC}^{max})}{\chi_T(H_{DC}^{max})} \times 100\%$, where $\chi_T(H_{DC}^{max})$ is the value of χ_T at the maximum value of the applied DC magnetic field, H_{DC}^{max} which is chosen in such a way that $H_{DC}^{max} \gg H_{DC}^{sat}$, where H_{DC}^{sat} is the saturation magnetic field. **Fig. 3(e)** shows the bipolar field scan ($+H_{DC}^{max} \rightarrow -H_{DC}^{max} \rightarrow +H_{DC}^{max}$) of $\frac{\Delta\chi_T}{\chi_T}(H_{DC})$ for MgO/CoFeCrGa film measured at $T = 20 \text{ K}$ for both IP (H_{DC} is parallel to the film surface) and OOP (H_{DC} is perpendicular to the film surface) configurations. For both the configurations, the TS shows maxima centering at $H_{DC} = \pm H_K^{eff}$. Here, we define $H_K^{eff} = H_K^{IP}$ as the IP effective anisotropy field (for IP configuration) and $H_K^{eff} = H_K^{OOP}$ as the OOP effective anisotropy field (for OOP configuration). We found that

$|H_K^{OOP}| > |H_K^{IP}|$ at all the temperatures indicating IP easy axis of this film in the temperature range: $20 \text{ K} \leq T \leq 300 \text{ K}$. Furthermore, it is evident that the peaks at $+H_K^{IP}$ ($+H_K^{OOP}$) and $-H_K^{IP}$ ($-H_K^{OOP}$) are asymmetric with unequal peak heights which is indicative of significant anisotropy dispersion in our MgO/CoFeCrGa film for the both IP and OOP configurations. The temperature variations of H_K^{IP} and H_K^{OOP} for our MgO/CoFeCrGa(95nm) film are shown in **Fig. 3(f)**. Clearly, both H_K^{IP} and H_K^{OOP} increase with decreasing temperature and $H_K^{OOP} > H_K^{IP}$ throughout the measured temperature range. Interestingly, with decreasing temperature, H_K^{OOP} increases more rapidly than H_K^{IP} which gives rise to large difference between H_K^{IP} and H_K^{OOP} at low temperatures. Additionally, both H_K^{IP} and H_K^{OOP} increases more rapidly below $\approx 200 \text{ K}$ compared to the temperature range of $200 \text{ K} \leq T \leq 300 \text{ K}$.

3.3. Thermal spin transport properties: ANE and LSSE

Next, we focus on the thermo-spin transport properties of our MgO/CoFeCrGa(95nm) film. We have performed anomalous Nernst effect (ANE) and longitudinal spin Seebeck effect (LSSE) measurements on MgO/CoFeCrGa(95nm) and MgO/CoFeCrGa(95nm)/Pt(5nm) films, respectively. **Figs. 4(a)** and **(b)** demonstrate the schematic illustrations of our ANE and LSSE measurements. Both the ANE and LSSE measurements on MgO/CoFeCrGa(95nm) and MgO/CoFeCrGa(95nm)/Pt films, respectively were performed by sandwiching the film between two copper blocks and applying a temperature gradient (along the $+z$ -direction) that creates a temperature difference, ΔT between those copper blocks in presence of an external DC magnetic field applied along the x -direction. The thermally generated Nernst and LSSE voltages generated along the y -direction were recorded using a Keithley 2182a nanovoltmeter while scanning the DC magnetic field. According to the theory of thermally generated magnon-driven interfacial spin pumping mechanism, simultaneous application of a vertical (z -axis) temperature gradient ($\overline{\nabla T}$) and an external transverse dc magnetic field ($\overline{\mu_0 H}$) (x -axis) across

the MgO/CoFeCrGa(95nm)/Pt film gives rise to transverse spin current pumping from the CoFeCrGa layer into the Pt layer with the interfacial spin current density: $\vec{J}_S = \frac{G^{\uparrow\downarrow}}{2\pi} \frac{\gamma\hbar}{M_S V_a} k_B \vec{\nabla T}$ at the CoFeCrGa/Pt interface, where $G^{\uparrow\downarrow}$, \hbar , γ , M_S , V_a and k_B are the interfacial spin-mixing conductance, the reduced Planck's constant ($\hbar = \frac{h}{2\pi}$), the gyromagnetic ratio, the saturation magnetization of CoFeCrGa, the magnon coherence volume and the Boltzmann constant, respectively^{42,65,66}. The magnetic coherence volume is expressed as: $V_a = \frac{2}{3\zeta(5/2)} \left(\frac{4\pi D}{k_B T}\right)^{3/2}$; where, ζ is the Riemann Zeta function and D is the spin-wave stiffness constant^{65,66}. This transverse spin current, \vec{J}_S is then converted into charge current, $\vec{J}_C = \left(\frac{2e}{\hbar}\right) \theta_{SH}^{Pt} (\vec{J}_S \times \vec{\sigma}_S)$ along the y-axis via the inverse spin Hall effect (ISHE), where e , θ_{SH}^{Pt} , and $\vec{\sigma}_S$ are the electron charge, the spin Hall angle of Pt, and the spin-polarization vector, respectively. The corresponding voltage along the y-axis can be expressed as,^{42,67,68}

$$V_{LSSE} = R_y L_y \lambda_{Pt} \left(\frac{2e}{\hbar}\right) \theta_{SH}^{Pt} J_S \tanh\left(\frac{t_{Pt}}{2\lambda_{Pt}}\right), \quad (1)$$

where R_y , L_y , λ_{Pt} , and t_{Pt} are the electrical resistance between the voltage leads, the distance between the voltage leads, the spin diffusion length of Pt, and the thickness of Pt layer (= 5 nm), respectively. Since CoFeCrGa is a spin-gapless semiconductor with soft ferromagnetic behavior,^{51,60} concomitant application of the temperature gradient (z -axis) and dc magnetic field (x -axis) also generates a spin-polarized current in the CoFeCrGa layer along the y-axis due to ANE,⁶⁹ which gives rise to an additional contribution ($V_{CoFeCrGa}^{ANE}$) to the total voltage signal measured across the Pt layer in the MgO/CoFeCrGa(95nm)/Pt heterostructure.

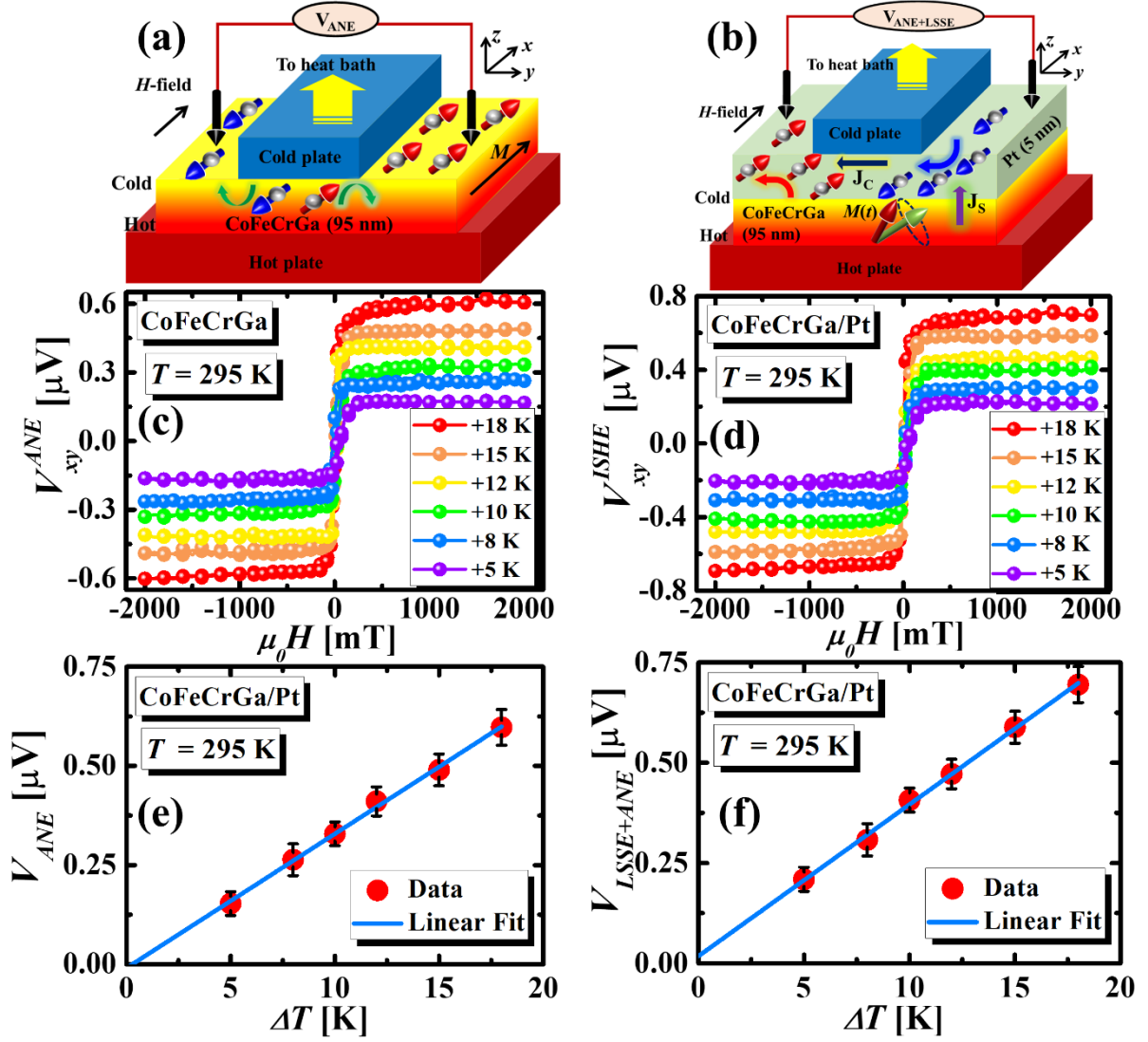


Figure 4. (a) and (b) the schematic illustrations of our ANE and LSSE measurements, respectively. (c) and (d) show the magnetic field dependence of the ANE voltage, $V_{ANE}(H)$ and ISHE-induced in-plane voltage, $V_{ISHE}(H)$ measured on the MgO/CoFeCrGa(95nm) and MgO/CoFeCrGa(95nm)/Pt films, respectively for different values of the temperature difference between the hot (T_{hot}) and cold (T_{cold}) copper blocks, $\Delta T = (T_{hot} - T_{cold})$ in the range: $+5 \text{ K} \leq \Delta T \leq +18 \text{ K}$ at a fixed average sample temperature $T = \frac{T_{hot} + T_{cold}}{2} = 295 \text{ K}$. (e) and (f) exhibit the ΔT dependence of the background-corrected ANE voltage, $V_{ANE}(\Delta T) = \left[\frac{V_{ANE}(+\mu_0 H_{max}, \Delta T) - V_{ANE}(-\mu_0 H_{max}, \Delta T)}{2} \right]$ and the background-corrected (ANE+LSSE) voltage, $V_{ANE+LSSE}(\Delta T) = \left[\frac{V_{ISHE}(+\mu_0 H_{max}, \Delta T) - V_{ISHE}(-\mu_0 H_{max}, \Delta T)}{2} \right]$, respectively.

In presence of a transverse temperature gradient (∇T), the electric field generated by ANE in a magnetic conductor/semiconductor with magnetization \vec{M} can be expressed as,¹⁵

$$\vec{E}_{ANE} \propto S_{ANE}(\mu_0 \vec{M} \times \nabla T) \quad (2)$$

where, S_{ANE} is the anomalous Nernst coefficient. Furthermore, an additional voltage contribution (V_{Prox}^{ANE}) can appear due to the magnetic proximity effect (MPE) induced ANE in the non-magnetic Pt layer.^{69,70} Note that, only a few layers of Pt close to the CoFeCrGa(95nm)/Pt interface gets magnetized (proximitized) due to the MPE, whereas the remaining layers remain unmagnetized. Hence both $V_{CoFeCrGa}^{ANE}$ and V_{Prox}^{ANE} are suppressed due to the inclusion of the 5 nm thick Pt layer on the top of CoFeCrGa layer.⁴¹ Therefore, the resultant voltage measured across the Pt layer of our MgO/CoFeCrGa(95nm)/Pt heterostructure can be expressed as,⁷¹ $V_{ANE+LSSE} = V_{LSSE} + V_{CoFeCrGa, Sup}^{ANE} + V_{Prox, Sup}^{ANE}$; where, $V_{CoFeCrGa, Sup}^{ANE}$ and $V_{Prox, Sup}^{ANE}$ account for the suppressed ANE voltages due to the CoFeCrGa layer and the MPE-induced ANE voltage in the Pt layer, respectively. Previous studies show that the contribution from the MPE-induced ANE in the Pt layer is negligibly small for bilayers consisting of magnetic semiconductors and Pt.^{41,69} Also, in our previous report,⁷¹ we have shown that the MPE-induced LSSE contribution of the proximitized Pt layer is negligible as only a few layers of Pt close to the CoFeCrGa(95nm)/Pt interface are magnetized due to the MPE⁴¹. Therefore, the resultant voltage measured across the Pt layer of our MgO/CoFeCrGa(95nm)/Pt heterostructure can be expressed as: $V_{ANE+LSSE} = V_{LSSE} + V_{CoFeCrGa, Sup}^{ANE}$. Considering a parallel circuit configuration of CoFeCrGa and Pt layers, the suppressed ANE voltage (due to the CoFeCrGa layer) across the Pt layer of the MgO/CoFeCrGa(95nm)/Pt heterostructure can be expressed as,^{41,69}

$$V_{CoFeCrGa, Sup}^{ANE} = \left(\frac{F}{1+F} \right) V_{CoFeCrGa}^{ANE} \quad (3)$$

where, $F = \frac{\rho_{Pt}}{\rho_{CoFeCrGa}} \cdot \frac{t_{CoFeCrGa}}{t_{Pt}}$, $\rho_{CoFeCrGa}$ (ρ_{Pt}) is the electrical resistivity of the CoFeCrGa (Pt) layer, and $t_{CoFeCrGa}$ (t_{Pt}) is the thickness of the CoFeCrGa (Pt) layer, respectively. Therefore, the intrinsic LSSE voltage contribution can be disentangled from the ANE contribution using the expression,^{41,71}

$$V_{LSSE} = V_{ANE+LSSE} - \left(\frac{F}{1+F} \right) V_{CoFeCrGa}^{ANE} \quad (4)$$

Figs. 4(c) and (d) show the magnetic field dependence of the ANE voltage, $V_{ANE}(H)$ and ISHE-induced in-plane voltage, $V_{ISHE}(H)$ measured on the MgO/CoFeCrGa(95nm) and MgO/CoFeCrGa(95nm)/Pt films, respectively for different values of the temperature difference between the hot (T_{hot}) and cold (T_{cold}) copper blocks, $\Delta T = (T_{hot} - T_{cold})$ in the range: $+5 \text{ K} \leq \Delta T \leq +18 \text{ K}$ at a fixed average sample temperature $T = \frac{T_{hot} + T_{cold}}{2} = 295 \text{ K}$. Clearly, both $V_{ANE}(H)$ and $V_{ISHE}(H)$ signals increase upon increasing ΔT . **Figs. 4**(e) and (f) exhibit the ΔT dependence of the background-corrected ANE voltage, $V_{ANE}(\Delta T) = \left[\frac{V_{ANE}(+\mu_0 H_{max}, \Delta T) - V_{ANE}(-\mu_0 H_{max}, \Delta T)}{2} \right]$ and the background-corrected (ANE+LSSE) voltage, $V_{ANE+LSSE}(\Delta T) = \left[\frac{V_{ISHE}(+\mu_0 H_{max}, \Delta T) - V_{ISHE}(-\mu_0 H_{max}, \Delta T)}{2} \right]$, respectively, where $\mu_0 H_{max}$ ($\mu_0 H_{max} \gg \mu_0 H_{sat}$) is the maximum value of the applied magnetic field strength and $\mu_0 H_{sat}$ = saturation magnetic field. Evidently, both V_{ANE} and $V_{ANE+LSSE}$ scale linearly with ΔT and $|V_{ANE+LSSE}| > |V_{ANE}|$, which confirm that the observed field dependences originate from the ANE and (ANE+LSSE), respectively^{41,71}.

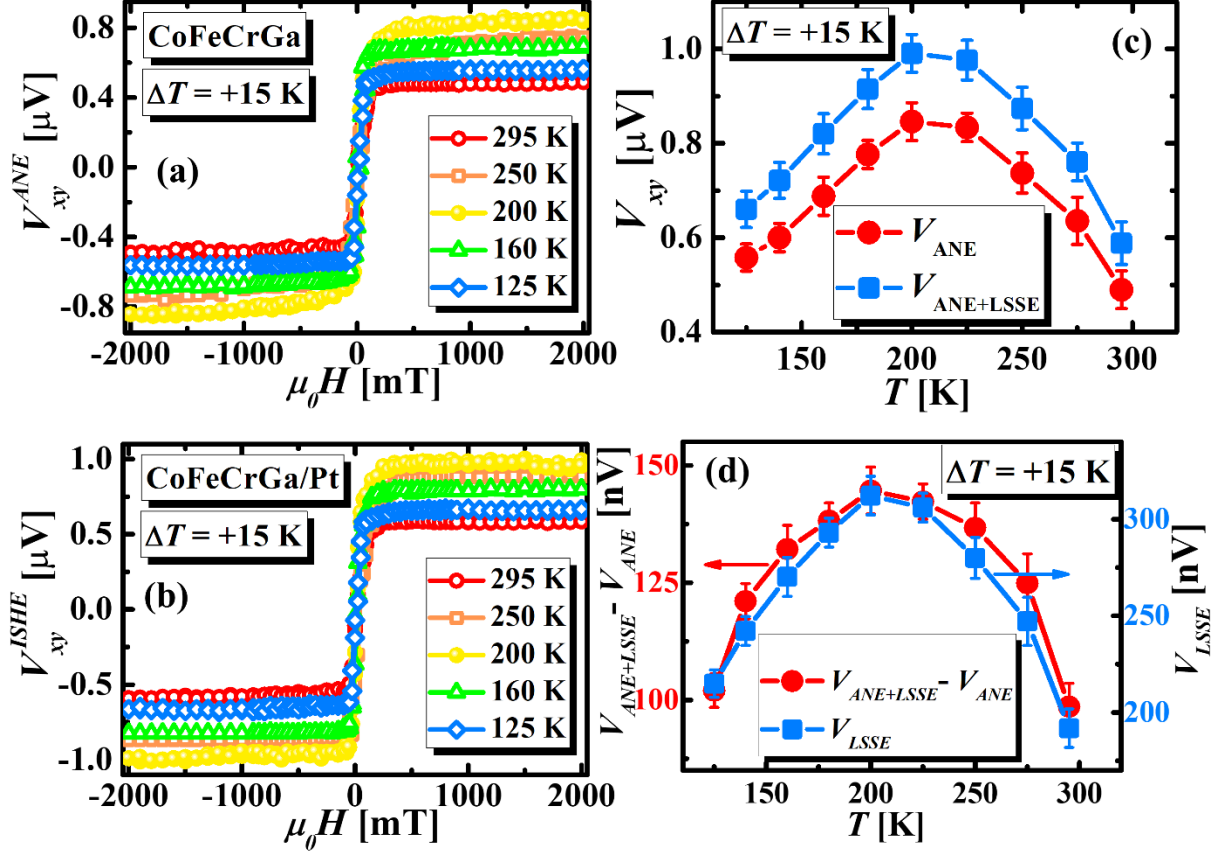


Figure 5. (a) and (b) $V_{ANE}(H)$ and $V_{ISHE}(H)$ hysteresis loops measured at selected average sample temperatures in the temperature range: $125 \text{ K} \leq \Delta T \leq 295 \text{ K}$ for a fixed value of $\Delta T = +15 \text{ K}$ on MgO/CoFeCrGa(95nm) and MgO/CoFeCrGa(95nm)/Pt films, respectively. (c) The T -dependence of the background-corrected ANE voltage, $V_{ANE}(T) = \left[\frac{V_{ANE}(+\mu_0 H_{max}, T) - V_{ANE}(-\mu_0 H_{max}, T)}{2} \right]$ and the background-corrected (ANE+LSSE) voltage, $V_{ANE+LSSE}(T) = \left[\frac{V_{ISHE}(+\mu_0 H_{max}, T) - V_{ISHE}(-\mu_0 H_{max}, T)}{2} \right]$ measured on MgO/CoFeCrGa(95nm) and MgO/CoFeCrGa(95nm)/Pt films, respectively. (d) Right y-scale: the temperature dependence of the intrinsic LSSE voltage, $V_{LSSE}(T)$ and the left y-scale: the temperature dependence of $[V_{ANE+LSSE}(T) - V_{ANE}(T)]$.

In **Figs. 5(a)** and **(b)**, we show $V_{ANE}(H)$ and $V_{ISHE}(H)$ hysteresis loops measured at selected average sample temperatures in the temperature range: $125 \text{ K} \leq \Delta T \leq 295 \text{ K}$ for a fixed value of $\Delta T = +15 \text{ K}$ on MgO/CoFeCrGa(95nm) and MgO/CoFeCrGa(95nm)/Pt films, respectively. **Fig. 5(c)** exhibits the T -dependence of the background-corrected ANE

voltage, $V_{ANE}(T) = \left[\frac{V_{ANE}(+\mu_0 H_{max}, T) - V_{ANE}(-\mu_0 H_{max}, T)}{2} \right]$ and the background-corrected (ANE+LSSE) voltage, $V_{ANE+LSSE}(T) = \left[\frac{V_{ISHE}(+\mu_0 H_{max}, T) - V_{ISHE}(-\mu_0 H_{max}, T)}{2} \right]$ measured on MgO/CoFeCrGa(95nm) and MgO/CoFeCrGa(95nm)/Pt films, respectively. It is evident that both $|V_{ANE}(T)|$ and $|V_{ANE+LSSE}(T)|$ increase with decreasing temperature up to $T = 200$ K below which both of them decrease gradually with further reducing the temperature, resulting in a maximum around 200 K. Furthermore, $|V_{ANE+LSSE}(T)| > |V_{ANE}(T)|$ throughout the measured temperature range, which confirms that both ANE and LSSE contribute towards the voltage measured on the MgO/CoFeCrGa(95nm)/Pt heterostructure.

In order to determine the temperature dependence of intrinsic LSSE voltage, we have disentangled the LSSE contribution from the ANE contribution using [Eqn. 4](#). The right y-scale of [Fig. 5\(d\)](#) shows the temperature dependence of the intrinsic LSSE voltage, $V_{LSSE}(T)$ obtained by using by [Eqn. 4](#) incorporating the correction factor: $\left(\frac{F}{1+F} \right)$, whereas the left y-scale shows the temperature dependence of the voltage difference $[V_{ANE+LSSE}(T) - V_{ANE}(T)]$ without incorporating the aforementioned correction factor, for comparison. A clear distinction can be observed between $V_{LSSE}(T)$ and $[V_{ANE+LSSE}(T) - V_{ANE}(T)]$ in terms of the absolute value as well the nature of the T -dependence, highlighting the importance of the correction factor for accurately determining the intrinsic LSSE contribution. Evidently, $|V_{LSSE}(T)|$ increases with decreasing temperature and shows a broad maximum around 200 K below which it decreases gradually with further lowering the temperature, as shown in [Fig. 5\(d\)](#). To ensure that the observed behavior of $V_{ANE}(T)$ and $V_{LSSE}(T)$ are intrinsic to the MgO/CoFeCrGa(95nm) and MgO/CoFeCrGa(95nm)/Pt films, respectively, we repeated the same experiments for two more CoFeCrGa films with different thicknesses, namely, $t_{\text{CoFeCrGa}} = 50$ and 200 nm.

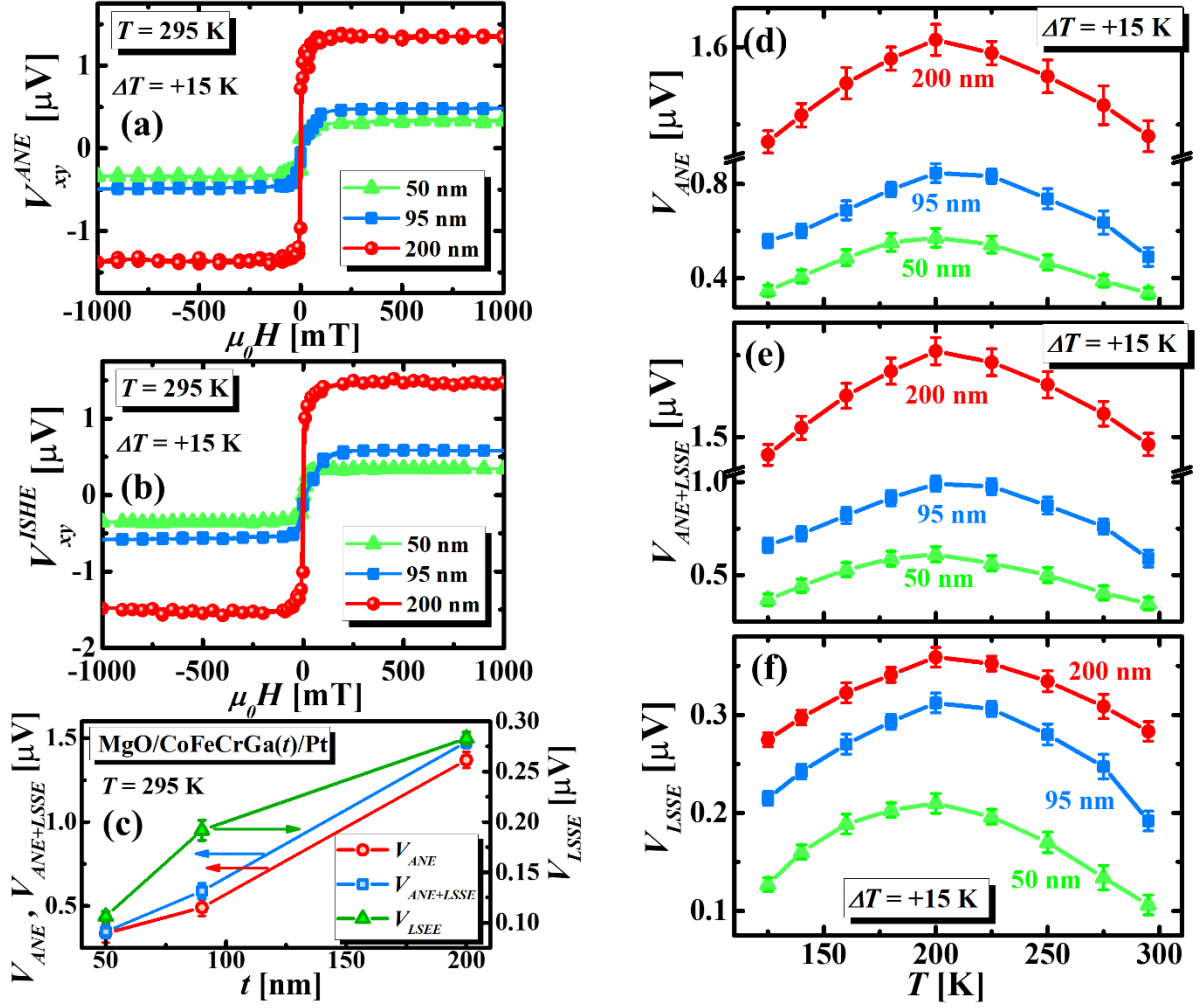


Figure 6. (a) and (b) $V_{ANE}(H)$ and $V_{ISHE}(H)$ hysteresis loops measured on the MgO/CoFeCrGa(t_{CoFeCrGa}) and MgO/CoFeCrGa(t_{CoFeCrGa})/Pt films for t_{CoFeCrGa} (CoFeCrGa film thickness) = 50, 95 and 200 nm at 295 K for $\Delta T = +15 \text{ K}$. (c) $V_{ANE}(\mu_0 H = 1 \text{ T})$, $V_{ANE+LSSE}(\mu_0 H = 1 \text{ T})$ and $V_{LSSE}(\mu_0 H = 1 \text{ T})$ at 295 K plotted as a function of t_{CoFeCrGa} . (d), (e) and (f) show the comparison of $V_{ANE}(T)$, $V_{ANE+LSSE}(T)$ and $V_{LSSE}(T)$, respectively for different t_{CoFeCrGa} .

The temperature dependent magnetometry and DC electrical transport properties of the $t_{\text{CoFeCrGa}} = 50$ and 200 nm films are displayed in the supplementary information (**Figures S1** and **S3**). Furthermore, similar to the $t_{\text{CoFeCrGa}} = 95 \text{ nm}$ film, both V_{ANE} and $V_{ANE+LSSE}$ for $t_{\text{CoFeCrGa}} = 50$ and 200 nm films scale linearly with ΔT and $|V_{ANE+LSSE}| > |V_{ANE}|$, as shown in **Figure S5**. In **Figure S6**, we demonstrate $V_{ANE}(H)$ and $V_{ISHE}(H)$ hysteresis loops at selected average sample temperatures in the range: $125 \text{ K} \leq \Delta T \leq 295 \text{ K}$ for a fixed value of

$\Delta T = +15$ K for $t_{\text{CoFeCrGa}} = 50$ and 200 nm films. In **Figs. 6(a)** and **(b)**, we compare $V_{ANE}(H)$ and $V_{ISHE}(H)$ hysteresis loops measured on the MgO/CoFeCrGa(t_{CoFeCrGa}) and MgO/CoFeCrGa(t_{CoFeCrGa})/Pt films for t_{CoFeCrGa} (CoFeCrGa film thickness) = 50, 95 and 200 nm at $T = 295$ K for $\Delta T = +15$ K. As shown in **Figs. 6(c)**, $V_{ANE}(\mu_0 H = 1 \text{ T})$, $V_{ANE+LSSE}(\mu_0 H = 1 \text{ T})$ and $V_{LSSE}(\mu_0 H = 1 \text{ T})$ at 295 K increase with increasing t_{CoFeCrGa} . In **Figs. 6(d)**, **(e)** and **(f)**, we compare $V_{ANE}(T)$, $V_{ANE+LSSE}(T)$ and $V_{LSSE}(T)$, respectively for different t_{CoFeCrGa} . Clearly, the values of all the three quantities: V_{ANE} , $V_{ANE+LSSE}$ and V_{LSSE} are higher for thicker CoFeCrGa films at all temperatures. Furthermore, $|V_{ANE}(T)|$, $|V_{ANE+LSSE}(T)|$ and $|V_{LSSE}(T)|$ exhibit the same behavior for all the three different CoFeCrGa film thicknesses, *i.e.*, all these quantities increase with decreasing temperature from 295 K and show a broad maximum around 200 K, which is followed by a gradual decrease with further lowering the temperature. These observations confirm that the observed behavior of $V_{ANE}(T)$ and $V_{LSSE}(T)$ are intrinsic to the MgO/CoFeCrGa and MgO/CoFeCrGa/Pt films, respectively.

3.4. Mechanism of LSSE and ANE at low temperatures

Since the density of the thermally generated magnons-driven spin current is proportional to the effective temperature gradient across the CoFeCrGa film through the expression, $|\vec{J}_S| = \frac{G^{\uparrow\downarrow}}{2\pi} \frac{\gamma\hbar}{M_S V_a} k_B |\nabla T|$, it is imperative to accurately determine the effective temperature differences between the top and bottom surfaces of the CoFeCrGa film (ΔT_{eff}). The total temperature difference (ΔT) across the MgO/CoFeCrGa/Pt heterostructure can be expressed as a linear combination of temperature drops in the Pt layer, at the Pt/CoFeCrGa interface, in the CoFeCrGa layer, at the CoFeCrGa/MgO interface, across the GSGG substrate as well as in the N-grease layers (thickness $\approx 1 \mu\text{m}$) on both sides of the MgO/CoFeCrGa/Pt

heterostructure, and can be written as,⁷² $\Delta T = \Delta T_{Pt} + \Delta T \frac{Pt}{CoFeCrGa} + \Delta T_{CoFeCrGa} + \Delta T_{MgO} + 2 \cdot \Delta T_{N-Grease}$. Since the thermal resistance of Pt is very small compared to the other contributions and the bulk contributions towards the measured ISHE voltage dominate over the interfacial contributions when the thickness of the magnetic film (CoFeCrGa) is high enough,⁷² the total temperature difference can be approximately written as,

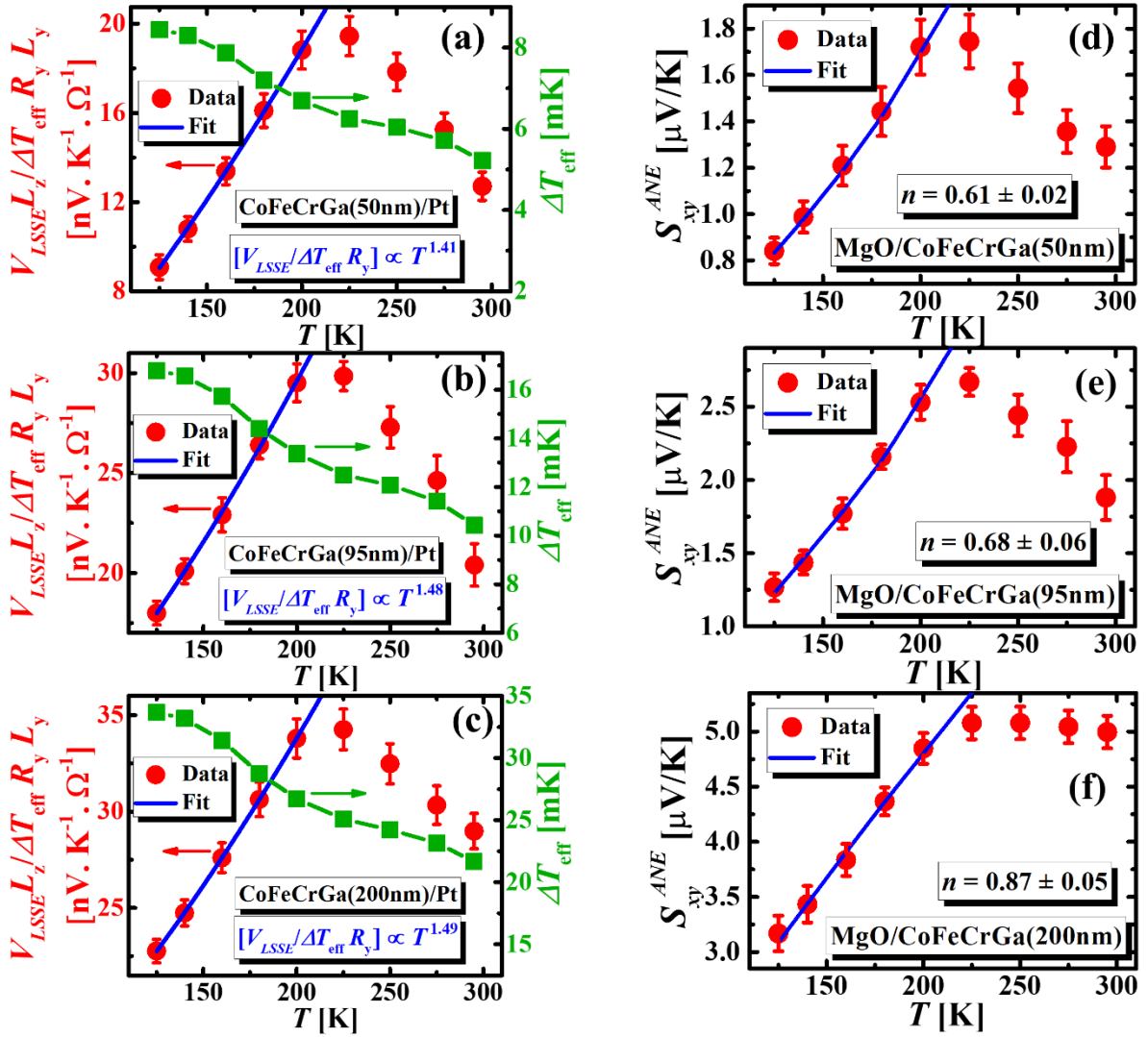
$$\Delta T = \Delta T_{CoFeCrGa} + \Delta T_{MgO} + 2 \cdot \Delta T_{N-Grease}.$$


Figure 7. (a)-(c) Right y-scale: temperature dependence of ΔT_{eff} for different $t_{CoFeCrGa}$, left y-scale: temperature dependence of the modified LSSE coefficient, $S_{LSSE}^{eff}(T)$ for MgO/CoFeCrGa($t_{CoFeCrGa}$)/Pt(5nm) films for $t_{CoFeCrGa} = 50, 95$ and 200 nm, respectively, fitted with the expression $S_{LSSE}^{eff} \propto \left(\theta_{SH}^{Pt} \frac{G^{\uparrow\downarrow}}{2\pi} \frac{k_B}{D^{3/2}} \right) T^n$. (d)-(f) Temperature dependence of the

ANE coefficient, $S_{xy}^{ANE}(T)$ for the MgO/CoFeCrGa(t_{CoFeCrGa}) films for $t_{\text{CoFeCrGa}} = 50, 95$ and 200 nm, respectively, fitted with [Eqn. 6](#).

Considering the 4-slab model, the total thermal resistance between hot and cold plates can be written as, $R_{Th} = \frac{1}{A} \left(\frac{2t_{N-Grease}}{\kappa_{N-Grease}} + \frac{t_{\text{CoFeCrGa}}}{\kappa_{\text{CoFeCrGa}}} + \frac{t_{\text{MgO}}}{\kappa_{\text{MgO}}} \right)$, where, $t_{N-Grease}$, t_{MgO} and t_{CoFeCrGa} are the thicknesses of the grease layers, MgO substrate and the CoFeCrGa layer, respectively; $\kappa_{N-Grease}$, κ_{MgO} and κ_{CoFeCrGa} are the thermal conductivities of the grease layers, MgO substrate and the CoFeCrGa layer, respectively, and A is the cross sectional area. Since the rate of heat flow across the entire heterostructure reaches a constant value in the steady state, the effective temperature difference across the CoFeCrGa film can be written as,⁴²

$$\Delta T_{eff} = \Delta T_{\text{CoFeCrGa}} = \frac{\Delta T}{\left[1 + \frac{\kappa_{\text{CoFeCrGa}}}{t_{\text{CoFeCrGa}}} \left(\frac{2t_{N-Grease}}{\kappa_{N-Grease}} + \frac{t_{\text{MgO}}}{\kappa_{\text{MgO}}} \right) \right]} \quad (5)$$

We have measured the temperature dependence of thermal conductivity of bulk CoFeCrGa using the thermal transport option of the PPMS, as shown in the supplementary information ([Figure S4](#)). Using the reported values of the thermal conductivities of the Apiezon N-grease,⁷³ and the MgO crystal⁷⁴, we have determined the temperature dependence of ΔT_{eff} for different t_{CoFeCrGa} using [Eqn. 5](#), as shown in [Figs. 7\(a\)-\(c\)](#). Here, we have ignored the interfacial thermal resistances between the N-grease and the hot/cold plates as well as between the sample and N-grease layers.¹⁴

Using the T -dependence of ΔT_{eff} , we have estimated the T -dependence of the modified LSSE coefficient, $S_{LSSE}^{eff}(T) = \frac{V_{LSSE}(T)}{\Delta T_{eff}(T)R_y(T)} \times \left(\frac{L_z}{L_y} \right)$ for MgO/CoFeCrGa(t_{CoFeCrGa})/Pt(5nm) films for $t_{\text{CoFeCrGa}} = 50, 95$ and 200 nm; where, L_y ($= 3$ mm) is the distance between the voltage leads and $L_z = t_{\text{CoFeCrGa}}$ (see [Figs. 7\(a\)-\(c\)](#)). Note that we have measured the T -dependence of resistance ($R_y(T)$) between the voltage-leads placed on the Pt layer of the

MgO/CoFeCrGa(t_{CoFeCrGa})/Pt heterostructures using 4-point probe configuration. Note that the value of $S_{LSSE}^{eff}(T)$ for our MgO/CoFeCrGa(t_{CoFeCrGa})/Pt heterostructures are $\approx 12.8, 20.5$ and $29.8 \text{ nV} \cdot \text{K}^{-1} \cdot \Omega^{-1}$ at $T = 295 \text{ K}$ for $t_{\text{CoFeCrGa}} = 50, 95$ and 200 nm , respectively, which are higher than that of the half-metallic FM thin films of $\text{La}_{0.7}\text{Sr}_{0.3}\text{MnO}_3$ ($\approx 9 \text{ nV} \cdot \text{K}^{-1} \cdot \Omega^{-1}$ at room temperature)⁴³. As shown in **Figs. 7(a)-(c)**, $S_{LSSE}^{eff}(T)$ for the MgO/CoFeCrGa(t_{CoFeCrGa})/Pt(5nm) heterostructures for all the three CoFeCrGa film thicknesses increases as T decreases from room temperature and shows a peak around 225 K below which it decreases rapidly with further decrease in temperature. Since the saturation magnetization, $M_S \approx T^{-1}$ in the measured temperature range (as shown in **Fig. 3(a)**) and, $V_a \propto T^{-3/2}$, according to the theory of magnon-driven LSSE, $|\vec{J}_S| \propto \frac{G^{\uparrow\downarrow} k_B}{2\pi D^{3/2}} T^{5/2} |\nabla T|$.⁴² Considering $\tanh\left(\frac{t_{Pt}}{2\lambda_{Pt}}\right) \approx 1$ for our case and, $\lambda_{Pt} \propto T^{-1}$,⁷⁵ according to the **Eqn. 1**, the modified LSSE coefficient becomes $S_{LSSE}^{eff} = \frac{V_{LSSE}}{\Delta T_{eff} R_y L_y} \propto \left(\theta_{SH}^{Pt} \frac{G^{\uparrow\downarrow} k_B}{2\pi D^{3/2}}\right) T^{3/2}$.⁴² As shown in **Figs. 7(a)-(c)**, $S_{LSSE}^{eff}(T)$ varies as $T^{1.41 \pm 0.12}$, $T^{1.48 \pm 0.08}$ and $T^{1.49 \pm 0.1}$ for $t_{\text{CoFeCrGa}} = 50, 95$ and 200 nm , respectively in the measured temperature range, which are in good agreement with the theory of thermally generated magnon-driven interfacial spin pumping mechanism^{42,65,66}.

Now, let us understand the origin of ANE in our MgO/CoFeCrGa(t_{CoFeCrGa}) films. The transverse thermoelectric coefficient (S_{xy}) is expressed as, $S_{xy} = \left[\frac{\alpha_{xy} - S_{xx}\sigma_{xy}}{\sigma_{xx}}\right]$, where σ_{xx} and σ_{xy} are the longitudinal and transverse electrical conductivities which are defined as,^{9,18,22}

$$\sigma_{xx} = \left[\frac{\rho_{xx}}{(\rho_{xx})^2 + (\rho_{xy})^2}\right] \text{ and } \sigma_{xy} = \left[\frac{-\rho_{xy}}{(\rho_{xx})^2 + (\rho_{xy})^2}\right],$$

respectively. Also, α_{xy} and S_{xx} are the transverse thermoelectric conductivity and longitudinal Seebeck coefficient, which according

to the Mott's relations can be expressed as,^{9,15,76} $\alpha_{xy} = \frac{\pi^2 k_B^2 T}{3e} \left(\frac{\partial \sigma_{xy}}{\partial E} \right)_{E=E_F}$ and $S_{xx} = \frac{\pi^2 k_B^2 T}{3e \sigma_{xx}} \left(\frac{\partial \sigma_{xx}}{\partial E} \right)_{E=E_F}$, respectively, where E_F is the Fermi energy. Since ANE and anomalous Hall Effect (AHE) share the common physical origin and the AHE follows the power law connecting the anomalous Hall resistivity, ρ_{xy}^{AHE} with the longitudinal electrical resistivity, ρ_{xx} through the expression, $\rho_{xy}^{AHE} = \lambda M \rho_{xx}^n$,⁹ where λ is the spin-orbit coupling constant and n is a constant exponent, the anomalous Nernst coefficient can be expressed as,^{9,15}

$$S_{xy}^{ANE} = \rho_{xx}^{n-1} \left[\frac{\pi^2 k_B^2 T}{3e} \left(\frac{\partial \lambda}{\partial E} \right)_{E=E_F} - (n-1) \lambda S_{xx} \right]. \quad (6)$$

When $n = 1$, the extrinsic skew scattering is the predominant mechanism for the anomalous Nernst/Hall transport, whereas $n = 2$ indicates the intrinsic Berry curvature or, the extrinsic side jump dominated anomalous Nernst/Hall transport²⁵. Using the T-dependences of ANE voltage, $V_{ANE}(T)$ and ΔT_{eff} , we have estimated the T -dependence of the ANE coefficient, $S_{xy}^{ANE}(T) = \frac{V_{ANE}(T)}{\Delta T_{eff}(T)} \times \left(\frac{L_z}{L_y} \right)$ for the MgO/CoFeCrGa($t_{CoFeCrGa}$) films, as shown in **Figs. 7(d)**-**(f)**. Similar to the modified LSSE voltage, $V_{LSSE}^{eff}(T)$, $S_{xy}^{ANE}(T)$ for the MgO/CoFeCrGa($t_{CoFeCrGa}$) films for all the three CoFeCrGa film thicknesses also increases as T decreases from room temperature and shows a maximum around 225 K below which it decreases rapidly with further decrease in temperature. Interestingly, $S_{xy}^{ANE}(T)$ for the MgO/CoFeCrGa(200 nm) film increases slowly with decreasing temperature from the room temperature and the maximum around 225 K is much broader in contrast to the films with lower thicknesses.

Note that the values of S_{xy}^{ANE} for our MgO/CoFeCrGa($t_{CoFeCrGa}$) films are $\approx 1.28, 1.86$ and $4.9 \mu\text{V} \cdot \text{K}^{-1}$ at $T = 295$ K and $\approx 1.75, 2.63$ and $5.1 \mu\text{V} \cdot \text{K}^{-1}$ at 225 K, for $t_{CoFeCrGa} = 50, 95$ and 200 nm, respectively which are nearly two orders of magnitude higher

than that of the bulk polycrystalline sample of CoFeCrGa ($\approx 0.018 \mu\text{V} \cdot \text{K}^{-1}$ at 300 K)¹⁴ but, comparable to that of the magnetic Weyl semimetal Co₂MnGa thin films ($\approx 2 - 3 \mu\text{V} \cdot \text{K}^{-1}$ at 300 K)^{77,78}. We fitted the $S_{xy}^{ANE}(T)$ data in the temperature range $125 \text{ K} \leq T \leq 200 \text{ K}$ for our MgO/CoFeCrGa(t_{CoFeCrGa}) films using **Eqn. 6** considering λ , $\left(\frac{\partial\lambda}{\partial E}\right)_{E=E_F}$, and n as the fitting parameters. The best fit was obtained for $n = 0.61 \pm 0.02$, 0.68 ± 0.06 and 0.87 ± 0.05 , for $t_{\text{CoFeCrGa}} = 50, 95$ and 200 nm , respectively which implies that the origin of ANE in our MgO/CoFeCrGa(t_{CoFeCrGa}) films is dominated by the asymmetric skew scattering of charge carriers below 200 K²⁵. Note that, we have also observed skew-scattering dominated ANE in bulk polycrystalline sample of CoFeCrGa,¹⁴ for which $n \approx 0.78$.

Next, let us examine the temperature evolution of the anomalous off-diagonal thermoelectric conductivity, $\alpha_{xy}^{ANE}(T)$. To determine $\alpha_{xy}^{ANE}(T)$, we have performed the Hall measurements on the MgO/CoFeCrGa(t_{CoFeCrGa}) films. **Figs. 8(a)-(c)** present the magnetic field dependence of Hall resistivity $\rho_{xy}(H)$ of our MgO/CoFeCrGa(t_{CoFeCrGa}) films for $t_{\text{CoFeCrGa}} = 50, 95$ and 200 nm , respectively recorded at few selected temperatures in the range: $125 \text{ K} \leq T \leq 295 \text{ K}$. By subtracting the ordinary Hall effect (OHE) contribution from $\rho_{xy}(H)$, we determined the T -dependence of the anomalous Hall resistivity $\rho_{xy}^{AHE}(T)$. The left-y scales of **Figs. 8(d)-(f)** exhibit the T -dependence of the anomalous Hall conductivity,

$|\sigma_{xy}^{AHE}| = \left[\frac{\rho_{xy}^{AHE}}{(\rho_{xx})^2 + (\rho_{xy}^{AHE})^2} \right]$ of our MgO/CoFeCrGa(t_{CoFeCrGa}) films for $t_{\text{CoFeCrGa}} = 50, 95$ and 200 nm , respectively. Note that $|\sigma_{xy}^{AHE}(T)|$ for our MgO/CoFeCrGa(t_{CoFeCrGa}) films increases almost linearly with decreasing temperature, unlike UC_{0.8}Ru_{0.2}Al for which $|\sigma_{xy}^{AHE}|$ is nearly temperature independent at low temperatures⁷⁹. This implies that σ_{xy}^{AHE} for our MgO/CoFeCrGa(95nm) film is strongly dependent on the scattering rate, which further

supports that the extrinsic mechanisms (*e.g.*, asymmetric skew scattering) dominate the transverse thermoelectric response of our sample at low temperatures⁷⁹.

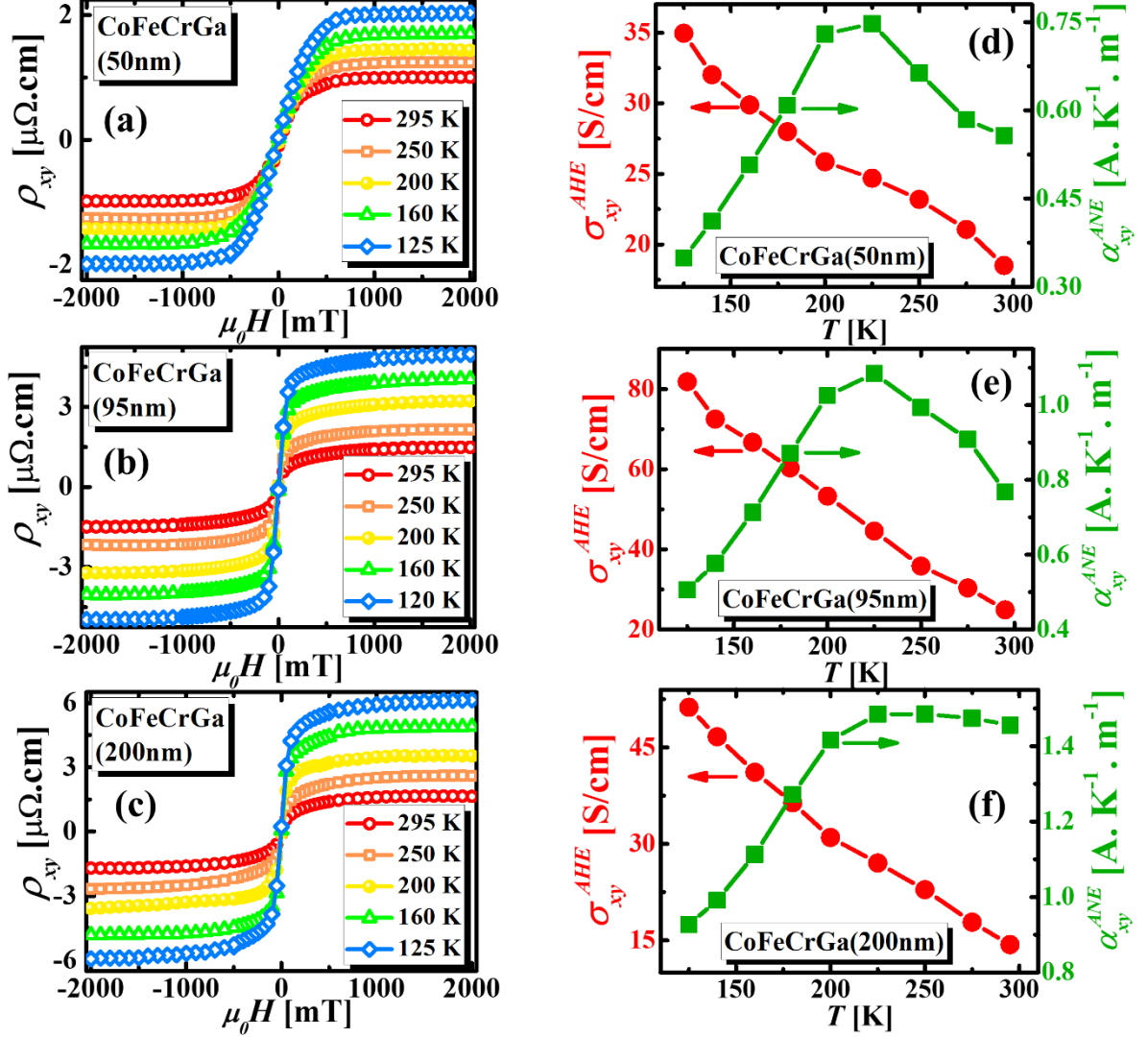


Figure 8. (a)-(c) Magnetic field dependence of Hall resistivity $\rho_{xy}(H)$ of our MgO/CoFeCrGa(t_{CoFeCrGa}) films for $t_{\text{CoFeCrGa}} = 50, 95$ and 200 nm, respectively recorded at few selected temperatures in the range: $125 \text{ K} \leq T \leq 295 \text{ K}$. (d)-(f) Left y-scale: the temperature dependence of the anomalous Hall conductivity, $|\sigma_{xy}^{AHE}|$ of our MgO/CoFeCrGa(t_{CoFeCrGa}) films for $t_{\text{CoFeCrGa}} = 50, 95$ and 200 nm, respectively, right y-scale: corresponding temperature variations of transverse thermoelectric conductivity α_{xy}^{ANE} .

The right y-scale of **Figs. 8(d)-(f)** illustrates the temperature variation of α_{xy}^{ANE} of our MgO/CoFeCrGa(t_{CoFeCrGa}) films for $t_{\text{CoFeCrGa}} = 50, 95$ and 200 nm, respectively, which was obtained by incorporating the T -dependences of S_{xx} , S_{ANE} , ρ_{xx} and ρ_{xy}^{AHE} in the expression,^{20,21,80} $\alpha_{xy}^{ANE} = S_{xy}^{ANE} \sigma_{xx} + S_{xx} \sigma_{xy}^{AHE} = \left[\frac{S_{xy}^{ANE} \rho_{xx} - S_{xx} \rho_{xy}^{AHE}}{(\rho_{xx})^2 + (\rho_{xy}^{AHE})^2} \right]$. It is evident that $\alpha_{xy}^{ANE}(T)$ for all the films shows a maximum around 225 K, similar to $S_{xy}^{ANE}(T)$. Note that similar to $S_{xy}^{ANE}(T)$, $\alpha_{xy}^{ANE}(T)$ for the MgO/CoFeCrGa(200 nm) film increases slowly with decreasing temperature from the room temperature and the maximum around 225 K is much broader in contrast to the films with lower thicknesses. The values of α_{xy}^{ANE} at room temperature (295 K) for our MgO/CoFeCrGa(t_{CoFeCrGa}) films are 0.55, 0.77 and 1.4 A. m⁻¹. K⁻¹ for $t_{\text{CoFeCrGa}} = 50, 95$ and 200 nm, respectively, which are much smaller than that of non-centrosymmetric Kagome ferromagnet UC_{0.8}Ru_{0.2}Al⁷⁹ (≈ 15 A. m⁻¹. K⁻¹ at 40 K), Co₂MnGa single crystal¹⁸ (≈ 7 A. m⁻¹. K⁻¹ at 300 K) but closer to that of Co₂MnGa thin films⁷⁸ (≈ 2 A. m⁻¹. K⁻¹ at 300 K).

Next, we focus on the origin of the maximum in both $S_{LSSE}^{eff}(T)$ and $S_{xy}^{ANE}(T)$ centered around 225 K. Note that the occurrence of maximum in both LSSE and ANE signals at the same temperature has been observed in other ferromagnetic metallic films, *e.g.*, mixed valent manganites⁴², iron oxides⁷¹. The maximum in the temperature dependent LSSE signal in the magnetically ordered state is commonly observed in different ferro- and ferrimagnets for example, YIG, La_{0.7}Ca_{0.3}MnO₃ etc., which originates as a consequence of the combined effects of boundary scattering and diffusive inelastic magnon-phonon or magnon-magnon scattering processes together with the reduction of magnon population at low temperatures^{33,42,81}. In YIG, the maximum in the LSSE signal is thickness dependent; it shifts from ≈ 70 K for bulk YIG slab to ≈ 200 K for 1 μm YIG film.³³ In ferromagnetic metals, extrinsic contributions arising

from electron-magnon scattering contributes significantly to the anomalous Nernst thermopower.⁴⁵ In presence of a temperature gradient and external magnetic field, magnons are excited in the bulk of a ferromagnetic material and these thermally generated magnons transfer spin-angular momenta to the itinerant electrons via electron-magnon scattering as a result of which the itinerant electrons of the ferromagnetic layer get spin polarized and contribute to the ANE.⁴⁵ Since the observed ANE in our MgO/CoFeCrGa(t_{CoFeCrGa}) films has dominating contribution from the extrinsic mechanism, the occurrence of maxima in $S_{xy}^{ANE}(T)$ around 225 K and the subsequent decrease in S_{xy}^{ANE} in our MgO/CoFeCrGa(t_{CoFeCrGa}) films can also be attributed to the diffusive inelastic magnon scatterings and reduced magnon population at low temperatures.⁴⁵ A decrease in the magnon population at low temperatures also reduces electron-magnon scattering which eventually diminishes the population of the spin-polarized itinerant electrons participating in the skew-scattering process.

In case of LSSE, the magnon propagation length ($\langle \xi \rangle$) of the ferromagnetic material also plays vital role in addition to the magnon population. $\langle \xi \rangle$ signifies the critical length scale for thermally-generated magnons to develop a spatial gradient of magnon accumulation inside a ferromagnetic film which is one of the crucial factors that governs spin angular momentum transfer to the adjacent HM layer^{31,33,82}. A decrease in $\langle \xi \rangle$ also suppresses the LSSE signal. It was theoretically shown that $\langle \xi \rangle$ of a magnetic material with lattice constant a_0 is related to the effective anisotropy constant (K_{eff}) and the Gilbert damping parameter (α), through the relation^{34,82} $\langle \xi \rangle = \frac{a_0}{2\alpha} \cdot \sqrt{\frac{J_{ex}}{2K_{eff}}}$, , where J_{ex} is the strength of the Heisenberg exchange interaction between nearest neighbors. Since $K_{eff} = \frac{1}{2} M_S H_K^{eff}$, the aforementioned expression can be written as, $\langle \xi \rangle = \frac{a_0}{2\alpha} \cdot \sqrt{\frac{J_{ex}}{\mu_0 M_S H_K^{eff}}}$. Thus, $\langle \xi \rangle$ is inversely proportional to α as

well as the square-root of $(M_S H_K^{eff})$. This implies that the T -evolution of $\langle \xi \rangle$ is related to that of α , H_K^{eff} and M_S . As shown in **Fig. 3(a)**, M_S for our MgO/CoFeCrGa(95nm) film increases with decreasing temperature. Furthermore, H_K^{eff} of our MgO/CoFeCrGa(95nm) film for both IP and OOP configurations (both H_K^{IP} and H_K^{OOP}) increases with decreasing temperature and the increase is more rapid below ≈ 200 K compared to the temperature range of $200 \text{ K} \leq T \leq 300 \text{ K}$, as indicated in **Fig. 3(f)**. Notably, similar behavior of H_K^{eff} has been observed for the MgO/CoFeCrGa(200nm) film (see **Figure S2**). Therefore, both H_K^{eff} and M_S tends to suppress $\langle \xi \rangle$ (and hence, S_{LSSE}^{eff}) at low temperatures, especially below ≈ 200 K. To comprehend the role of α in $\langle \xi \rangle$ and hence, the LSSE signal at low temperatures, we have investigated the spin-dynamic properties of our MgO/CoFeCrGa(95nm) and MgO/CoFeCrGa(95nm)/Pt(5nm) films by employing the broadband ferromagnetic resonance (FMR) measurements.

3.5. Magnetization dynamics and Gilbert damping

Figs. 9(a) and **(b)** display the field-derivative of microwave (MW) power absorption spectra $\left(\frac{dP}{dH}\right)$ as a function of the IP DC magnetic field for various frequencies in the range: $4 \text{ GHz} \leq f \leq 18 \text{ GHz}$ recorded at $T = 250 \text{ K}$ for the MgO/CoFeCrGa(95nm) and MgO/CoFeCrGa(95nm)/Pt(5nm) films, respectively. To extract the resonance field (H_{res}) and linewidth (ΔH), we fitted the $\frac{dP}{dH}$ lineshapes with a linear combination of symmetric and antisymmetric Lorentzian function derivatives as,⁸³

$$\frac{dP}{dH} = P_{Sym} \frac{\frac{\Delta H}{2}(H_{dc} - H_{res})}{\left[(H_{dc} - H_{res})^2 + \left(\frac{\Delta H}{2}\right)^2\right]^2} + P_{Asym} \frac{\left(\frac{\Delta H}{2}\right)^2 - (H_{dc} - H_{res})^2}{\left[(H_{dc} - H_{res})^2 + \left(\frac{\Delta H}{2}\right)^2\right]^2} + P_0 \quad (7)$$

where, P_{Sym} and P_{Asym} are the coefficients of the symmetric and antisymmetric Lorentzian derivatives, and P_0 is a constant offset parameter. The fitted curves are represented by solid lines in **Figs. 9(a)** and **(b)**. To obtain the temperature evolution of the damping parameter, $\alpha(T)$

for the MgO/CoFeCrGa(95nm) and MgO/CoFeCrGa(95nm)/Pt(5nm) films, we have fitted the ΔH - f curves with the expression,⁸⁴ $\Delta H = \Delta H_0 + \frac{4\pi\alpha}{\gamma\mu_0}f$, where, ΔH_0 represents the inhomogeneous broadening, $\frac{\gamma}{2\pi} = \frac{g_{eff}\mu_B}{\hbar}$ is the gyromagnetic ratio, μ_B is the Bohr magneton, g_{eff} is the Landé g -factor. **Figs. 9(c)** shows the ΔH - f curves for the MgO/CoFeCrGa(95nm) film at different temperatures fitted with the aforementioned expression. Clearly, the slope of the ΔH - f curves increases with decreasing temperature which implies increase α at low temperatures. In **Fig. 9(d)**, we compare the ΔH - f curves for the MgO/CoFeCrGa(95nm) and MgO/CoFeCrGa(95nm)/Pt(5nm) films recorded at $T = 250$ K. It is evident that ΔH for MgO/CoFeCrGa(95nm)/Pt(5nm) is higher than that of MgO/CoFeCrGa(95nm) for all the frequencies, which is because of the loss of spin angular momentum in the CoFeCrGa film as a result of spin pumping and can be expressed as,⁸⁵ $[\Delta H_{CoFeCrGa/Pt} - \Delta H_{CoFeCrGa}] = G_R^{\uparrow\downarrow} \left(\frac{g_{eff}\mu_B}{2\gamma M_S t_{CoFeCrGa}} \right) f$, where $G_R^{\uparrow\downarrow}$ is the real component of the interfacial spin mixing conductance ($G^{\uparrow\downarrow}$). From the fits, we obtained $\alpha_{CoFeCrGa} = (3.6 \pm 0.2) \times 10^{-2}$ and $\alpha_{CoFeCrGa/Pt} = (4.12 \pm 0.1) \times 10^{-2}$ at 250 K for the MgO/CoFeCrGa(95nm), and MgO/CoFeCrGa(95nm)/Pt(5nm) films, respectively. Clearly, $\alpha_{CoFeCrGa/Pt} > \alpha_{CoFeCrGa}$ which is caused by additional damping due to the spin pumping effect⁸⁵. In **Fig. 9(e)**, we compare $\alpha(T)$ for the MgO/CoFeCrGa(95nm), and MgO/CoFeCrGa(95nm)/Pt(5nm) films. It is evident that $\alpha_{CoFeCrGa/Pt} > \alpha_{CoFeCrGa}$ at all the temperatures and both $\alpha_{CoFeCrGa/Pt}$ and $\alpha_{CoFeCrGa}$ increase with decrease temperature, especially below 225 K. Such increase in α and ΔH at low temperatures can be primarily attributed to the impurity relaxation mechanisms^{86–88}. Since $\langle \xi \rangle \propto \frac{1}{\alpha}$, an increase in α at low temperatures gives rise to decrease in $\langle \xi \rangle$, and hence, the LSSE signal. The increases in ΔH_0 at low temperatures for both MgO/CoFeCrGa(95nm) MgO/

CoFeCrGa(95nm)/Pt(5nm) films (see right y-scale of Fig. 9(f)) also support the occurrence of impurity relaxation at low temperatures⁸⁹.

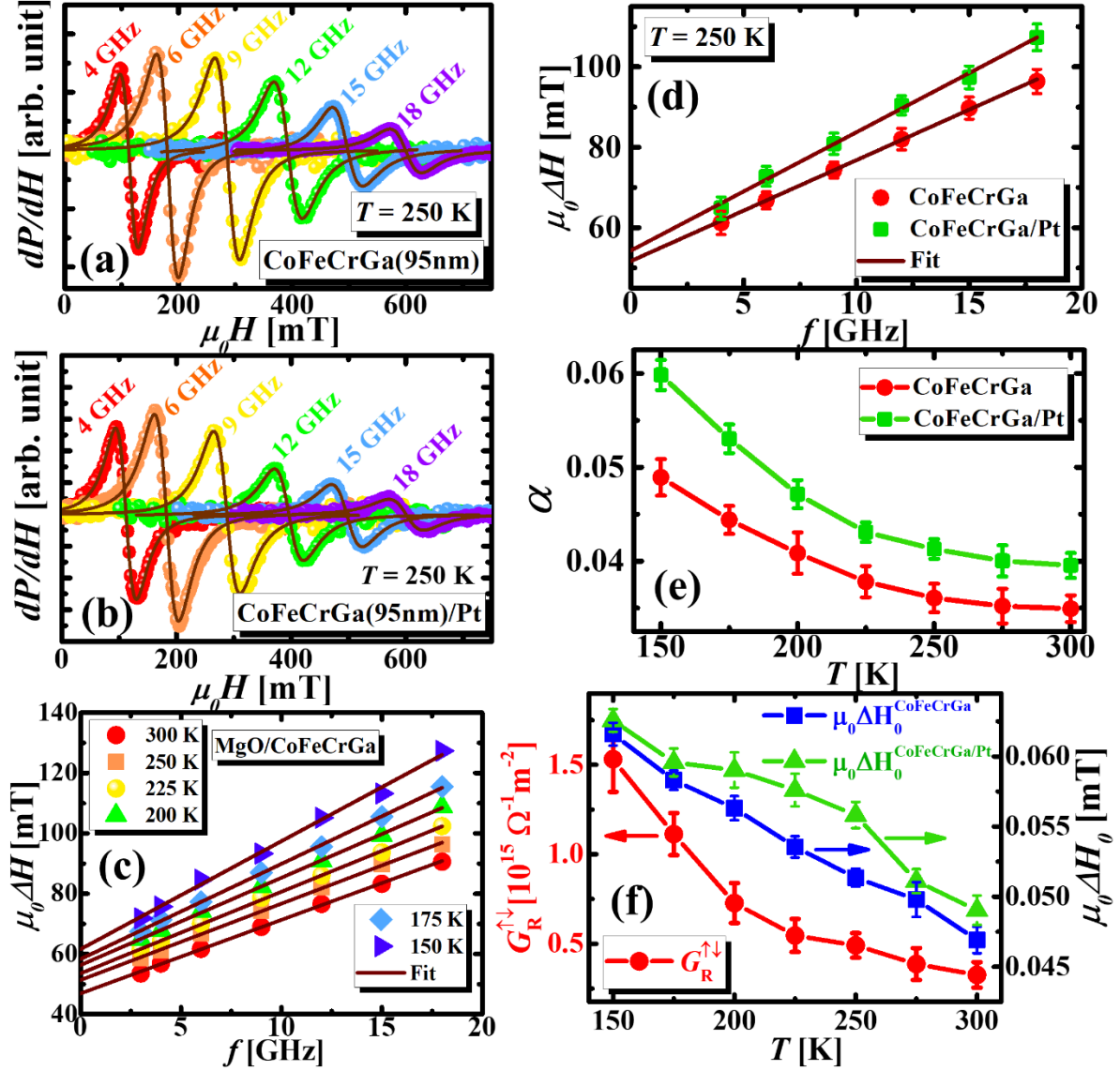


Figure 9. (a) and (b) Field-derivative of microwave (MW) power absorption spectra ($\frac{dP}{dH}$) as a function of the IP DC magnetic field for various frequencies in the range: $4 \text{ GHz} \leq f \leq 18 \text{ GHz}$ recorded at 250 K for the MgO/CoFeCrGa(95nm) and MgO/CoFeCrGa(95nm)/Pt(5nm) films, respectively fitted with Eqn. 7. (c) The ΔH - f curves for the MgO/CoFeCrGa(95nm) film at different temperatures fitted with $\Delta H = \Delta H_0 + \frac{4\pi\alpha}{\gamma\mu_0} f$. (d) The comparison of the ΔH - f curves for the MgO/CoFeCrGa(95nm) and MgO/CoFeCrGa(95nm)/Pt(5nm) films recorded at 250 K. (e) Comparison of the temperature dependence of damping parameter $\alpha(T)$ for the MgO/CoFeCrGa(95nm), and MgO/CoFeCrGa(95nm)/Pt(5nm) films. (f) Right y-scale: temperature dependence of ΔH_0 for the MgO/CoFeCrGa(95nm) and

MgO/CoFeCrGa(95nm)/Pt films, left y-scale: temperature dependence of the real component of the spin mixing conductance $G_R^{\uparrow\downarrow}$ for the MgO/CoFeCrGa(95nm)/Pt(5nm) film.

To have a quantitative understanding of the T -evolution of spin pumping efficiency in the MgO/CoFeCrGa(95nm)/Pt(5nm) film, we estimated $G_R^{\uparrow\downarrow}$ using the expression,⁹⁰ $G_R^{\uparrow\downarrow} = \left(\frac{2e^2}{h}\right) \left(\frac{2\pi M_{StCoFeCrGa}}{g_{eff}\mu_B}\right) [\alpha_{CoFeCrGa/Pt} - \alpha_{CoFeCrGa}]$ where, $G_0 = \left(\frac{2e^2}{h}\right)$ is the conductance quantum, and found that $G_R^{\uparrow\downarrow} \approx 3.25 \times 10^{14} \Omega^{-1}\text{m}^{-2}$ at 300 K which is close to $G_R^{\uparrow\downarrow} = 7.5 \times 10^{14} \Omega^{-1}\text{m}^{-2}$ in YIG/Pt⁹¹ and $G_R^{\uparrow\downarrow} = 5.7 \times 10^{14} \Omega^{-1}\text{m}^{-2}$ in TmIG/Pt bilayers⁹⁰. As shown in **Fig. 9**(d), $G_R^{\uparrow\downarrow}$ for the MgO/CoFeCrGa(95nm)/Pt(5nm) film increases with decreasing temperature, which is consistent with the phenomenological expression,⁹² $G_R^{\uparrow\downarrow} \propto (T_C - T)$, where T_C = Curie temperature. Furthermore, to confirm the aforementioned behavior of the temperature evolution of α , we have repeated the broadband FMR measurements on the MgO/CoFeCrGa(200nm)/Pt(5nm) film. **Figs. 10**(a) display the magnetic field dependence of the $\left(\frac{dP}{dH}\right)$ lineshapes in the range: $6 \text{ GHz} \leq f \leq 24 \text{ GHz}$ recorded at $T = 250 \text{ K}$ for the MgO/CoFeCrGa(200nm)/Pt film, fitted with **Eqn. 7**. To obtain the temperature evolution of the damping parameter, $\alpha(T)$ we have fitted the ΔH - f curves at different temperatures in the range of $140 \text{ K} \leq T \leq 300 \text{ K}$ with the expression,⁸⁴ $\Delta H = \Delta H_0 + \frac{4\pi\alpha}{\gamma\mu_0} f$, as shown in **Fig. 10**(b). Evidently, the slope of the ΔH - f curves increases with decreasing temperature which implies increase α at low temperatures. Moreover, in **Fig. 10**(c), we show the fitting of the f - H_{res} curves at $T = 250 \text{ K}$ using Kittel's equation for magnetic thin films with IP magnetic field,⁸⁶ which is expressed as, $f = \frac{\gamma\mu_0}{2\pi} \sqrt{H_{res}(H_{res} + M_{eff})}$, where M_{eff} is the effective magnetization.

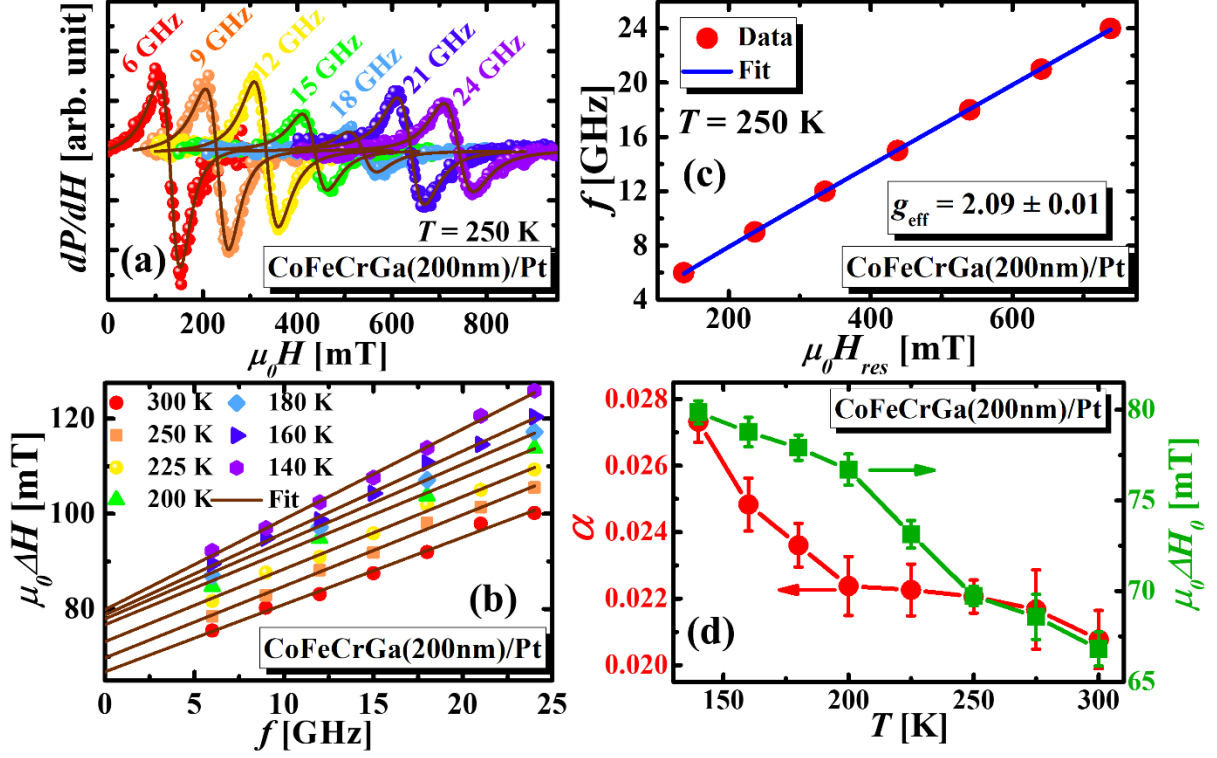


Figure 10. (a) Field-derivative of $\left(\frac{dP}{dH}\right)$ as a function of the IP DC magnetic field for various frequencies in the range: $6 \text{ GHz} \leq f \leq 24 \text{ GHz}$ recorded at $T = 250 \text{ K}$ for the MgO/CoFeCrGa(200nm)/Pt fitted with **Eqn. 7**. (b) The ΔH - f curves for the MgO/CoFeCrGa(200nm)/Pt film at different temperatures fitted with $\Delta H = \Delta H_0 + \frac{4\pi\alpha}{\gamma\mu_0} f$. (c) Fitting of the f vs. the resonance field, H_{res} using the Kittel's equation at $T = 250 \text{ K}$ for the MgO/CoFeCrGa(200nm)/Pt film. (d) Left y scale: temperature dependence of damping parameter $\alpha(T)$ for the MgO/CoFeCrGa(200nm)/Pt, and right y-scale: temperature dependence of ΔH_0 for the same.

The estimated value of $g_{eff} = (2.09 \pm 0.01)$ at 250 K for the MgO/CoFeCrGa(200nm)/Pt(5nm) film, which is slightly higher than the free electron value ($g_{eff} = 2.002$). Note that $g_{eff} = (2.046 \pm 0.01)$ and (2.048 ± 0.02) for the MgO/CoFeCrGa(95nm) and MgO/CoFeCrGa(95nm)/Pt(5nm) films, respectively at 250 K. Finally, $\alpha(T)$ for the MgO/CoFeCrGa(200nm)/Pt film is shown on the left y-axis of **Fig. 10(d)**. It is evident that $\alpha(T)$ increases with decreasing temperature, especially below 225 K similar to what we have observed for the MgO/CoFeCrGa(95nm) and MgO/

CoFeCrGa(95nm)/Pt(5nm) films. This observation further confirms the contribution of α towards the observed decrease in the LSSE signal in the CoFeCrGa films below the temperature range of 200-225 K.

4. CONCLUSIONS

In summary, we present a comprehensive investigation of the temperature ANE and intrinsic longitudinal spin Seebeck effect (LSSE) in the quaternary Heusler alloy based SGS thin films of CoFeCrGa grown on MgO substrates. We found that the anomalous Nernst coefficient for the MgO/CoFeCrGa (95 nm) film is $\approx 1.86 \mu\text{V} \cdot \text{K}^{-1}$ at room temperature which is much higher than the bulk polycrystalline sample of CoFeCrGa ($\approx 0.018 \mu\text{V} \cdot \text{K}^{-1}$ at 300 K) but comparable to that of the magnetic Weyl semimetal Co_2MnGa thin films ($\approx 2 - 3 \mu\text{V} \cdot \text{K}^{-1}$ at 300 K). Furthermore, the LSSE coefficient for our MgO/CoFeCrGa(95nm)/Pt(5nm) heterostructure is $\approx 20.5 \text{ nV} \cdot \text{K}^{-1} \cdot \Omega^{-1}$ at 295 K which is twice larger than that of the half-metallic ferromagnetic $\text{La}_{0.7}\text{Sr}_{0.3}\text{MnO}_3$ thin films ($\approx 9 \text{ nV} \cdot \text{K}^{-1} \cdot \Omega^{-1}$ at room temperature). We have shown that both ANE and LSSE coefficients follow identical temperature dependences and exhibit a maximum $\approx 225 \text{ K}$ which is understood as the combined effects of inelastic magnon scatterings and reduced magnon population at low temperatures. Our analyses not only indicated that the extrinsic skew scattering is the dominating mechanism for ANE in these films but also, provided critical insights into the functional form of the observed temperature dependent LSSE at low temperatures. Furthermore, by employing radio frequency transverse susceptibility and broadband ferromagnetic resonance in combination with the LSSE measurements, we have established a correlation among the observed LSSE signal, magnetic anisotropy and Gilbert damping of the CoFeCrGa thin films which will be beneficial for fabricating tunable and highly efficient spin caloritronic nanodevices. We believe that our findings will also attract the attention of materials science and spintronics community for

further exploration of different Heusler alloys based magnetic thin films and heterostructures co-exhibiting multiple thermo-spin effects with promising efficiencies.

ACKNOWLEDGEMENTS

HS and MHP acknowledge support from the US Department of Energy, Office of Basic Energy Sciences, Division of Materials Science and Engineering under Award No. DE-FG02-07ER46438. HS thanks the Alexander von Humboldt foundation for a research award and also acknowledges a visiting professorship at IIT Bombay. D.A.A. acknowledges the support of the National Science Foundation under Grant No. ECCS-1952957. DD and RC acknowledge the financial assistance received from DST Nanomission project (DST/NM/TUE/QM-11/2019).

SUPPORTING INFORMATION

Magnetometry, temperature dependence of electrical resistivity, magnetic field and temperature dependences of transverse susceptibility, magnetic field dependence of ANE and LSSE voltages for the MgO/CoFeCrGa (200 nm) and MgO/CoFeCrGa (50 nm) films.

DATA AVAILABILITY

The data that support the findings of this study are available from the corresponding author upon reasonable request.

REFERENCES

- (1) Bauer, G. E. W.; Saitoh, E.; Van Wees, B. J. Spin Caloritronics. *Nat. Mater.* **2012**, *11* (5), 391–399.
- (2) Uchida, K.-I. Transport Phenomena in Spin Caloritronics. *Proc. Japan Acad. Ser. B* **2021**, *97* (2), 69–88.
- (3) Sakai, A.; Mizuta, Y. P.; Nugroho, A. A.; Sihombing, R.; Koretsune, T.; Suzuki, M.-T.; Takemori, N.; Ishii, R.; Nishio-Hamane, D.; Arita, R.; others. Giant Anomalous Nernst Effect and Quantum-Critical Scaling in a Ferromagnetic Semimetal. *Nat. Phys.* **2018**, *14* (11), 1119–1124.
- (4) Meyer, S.; Chen, Y.-T.; Wimmer, S.; Althammer, M.; Wimmer, T.; Schlitz, R.; Geprägs, S.; Huebl, H.; Ködderitzsch, D.; Ebert, H.; others. Observation of the Spin Nernst Effect. *Nat. Mater.* **2017**, *16* (10), 977–981.
- (5) Uchida, K.; Takahashi, S.; Harii, K.; Ieda, J.; Koshibae, W.; Ando, K.; Maekawa, S.; Saitoh, E. Observation of the Spin Seebeck Effect. *Nature* **2008**, *455* (7214), 778–781.
- (6) Uchida, K.; Xiao, J.; Adachi, H.; Ohe, J.; Takahashi, S.; Ieda, J.; Ota, T.; Kajiwara, Y.; Umezawa, H.; Kawai, H. Spin Seebeck Insulator. *Nat. Mater.* **2010**, *9* (11), 894–897.
- (7) Daimon, S.; Iguchi, R.; Hioki, T.; Saitoh, E.; Uchida, K. Thermal Imaging of Spin Peltier Effect. *Nat. Commun.* **2016**, *7* (1), 13754.
- (8) Ikhlas, M.; Tomita, T.; Koretsune, T.; Suzuki, M.-T.; Nishio-Hamane, D.; Arita, R.; Otani, Y.; Nakatsuji, S. Large Anomalous Nernst Effect at Room Temperature in a Chiral Antiferromagnet. *Nat. Phys.* **2017**, *13* (11), 1085–1090.
- (9) Pu, Y.; Chiba, D.; Matsukura, F.; Ohno, H.; Shi, J. Mott Relation for Anomalous Hall and Nernst Effects in Ga_{1-x}Mn_xAs Ferromagnetic Semiconductors. *Phys. Rev. Lett.* **2008**, *101* (11), 117208.
- (10) Ghosh, A.; Das, R.; Mahendiran, R. Skew Scattering Dominated Anomalous Nernst

- Effect in $\text{La}_{1-x}\text{Na}_x\text{MnO}_3$. *J. Appl. Phys.* **2019**, *125* (15), 153902.
- (11) Ghosh, A.; Chanda, A.; Mahendiran, R. Anomalous Nernst Effect in PrO_5SrO_3 . *AIP Adv.* **2021**, *11* (3), 35031.
- (12) Ghosh, A.; Chanda, A.; Manikandan, M.; Mahendiran, R. Rare Earth Size Dependence of Nernst Thermopower in Ferromagnetic Perovskites: $\text{R}_0.6\text{Sr}_0.4\text{CoO}_3$ (R= La, Pr, and Nd). *J. Magn. Magn. Mater.* **2021**, *537*, 168240.
- (13) Miyasato, T.; Abe, N.; Fujii, T.; Asamitsu, A.; Onoda, S.; Onose, Y.; Nagaosa, N.; Tokura, Y. Crossover Behavior of the Anomalous Hall Effect and Anomalous Nernst Effect in Itinerant Ferromagnets. *Phys. Rev. Lett.* **2007**, *99* (8), 86602.
- (14) Chanda, A.; Rani, D.; Nag, J.; Alam, A.; Suresh, K. G.; Phan, M. H.; Srikanth, H. Emergence of Asymmetric Skew-Scattering Dominated Anomalous Nernst Effect in the Spin Gapless Semiconductors $\text{Co}_{1+x}\text{Fe}_{1-x}\text{CrGa}$. *Phys. Rev. B* **2022**, *106* (13), 134416.
- (15) Ramos, R.; Aguirre, M. H.; Anadón, A.; Blasco, J.; Lucas, I.; Uchida, K.; Algarabel, P. A.; Morellón, L.; Saitoh, E.; Ibarra, M. R. Anomalous Nernst Effect of Fe_3O_4 Single Crystal. *Phys. Rev. B* **2014**, *90* (5), 54422.
- (16) Isogami, S.; Masuda, K.; Miura, Y.; Rajamanickam, N.; Sakuraba, Y. Anomalous Hall and Nernst Effects in Ferrimagnetic Mn_4N Films: Possible Interpretations and Prospects for Enhancement. *Appl. Phys. Lett.* **2021**, *118* (9), 92407.
- (17) Sakuraba, Y.; Hyodo, K.; Sakuma, A.; Mitani, S. Giant Anomalous Nernst Effect in the $\text{Co}_2\text{MnAl}_{1-x}\text{Si}_x$ Heusler Alloy Induced by Fermi Level Tuning and Atomic Ordering. *Phys. Rev. B* **2020**, *101* (13), 134407.
- (18) Guin, S. N.; Manna, K.; Noky, J.; Watzman, S. J.; Fu, C.; Kumar, N.; Schnelle, W.; Shekhar, C.; Sun, Y.; Gooth, J.; others. Anomalous Nernst Effect beyond the Magnetization Scaling Relation in the Ferromagnetic Heusler Compound Co_2MnGa .

- NPG Asia Mater.* **2019**, *11* (1), 1–9.
- (19) Shukla, G. K.; Modanwal, U.; Singh, S. Nodal-Line Symmetry Breaking Induced Colossal Anomalous Hall and Nernst Effects in Cu₂CoSn Heusler Compound. *Appl. Phys. Lett.* **2023**, *123* (5).
- (20) Yang, H.; You, W.; Wang, J.; Huang, J.; Xi, C.; Xu, X.; Cao, C.; Tian, M.; Xu, Z.-A.; Dai, J.; others. Giant Anomalous Nernst Effect in the Magnetic Weyl Semimetal Co₃Sn₂S₂. *Phys. Rev. Mater.* **2020**, *4* (2), 24202.
- (21) Ding, L.; Koo, J.; Xu, L.; Li, X.; Lu, X.; Zhao, L.; Wang, Q.; Yin, Q.; Lei, H.; Yan, B.; others. Intrinsic Anomalous Nernst Effect Amplified by Disorder in a Half-Metallic Semimetal. *Phys. Rev. X* **2019**, *9* (4), 41061.
- (22) Xu, J.; Phelan, W. A.; Chien, C.-L. Large Anomalous Nernst Effect in a van Der Waals Ferromagnet Fe₃GeTe₂. *Nano Lett.* **2019**, *19* (11), 8250–8254.
- (23) Fang, C.; Wan, C. H.; Guo, C. Y.; Feng, C.; Wang, X.; Xing, Y. W.; Zhao, M. K.; Dong, J.; Yu, G. Q.; Zhao, Y. G.; others. Observation of Large Anomalous Nernst Effect in 2D Layered Materials Fe₃GeTe₂. *Appl. Phys. Lett.* **2019**, *115* (21), 212402.
- (24) Pan, Y.; Le, C.; He, B.; Watzman, S. J.; Yao, M.; Gooth, J.; Heremans, J. P.; Sun, Y.; Felser, C. Giant Anomalous Nernst Signal in the Antiferromagnet YbMnBi₂. *Nat. Mater.* **2022**, *21* (2), 203–209.
- (25) Nagaosa, N.; Sinova, J.; Onoda, S.; MacDonald, A. H.; Ong, N. P. Anomalous Hall Effect. *Rev. Mod. Phys.* **2010**, *82* (2), 1539.
- (26) Ghosh, A.; De, A.; Nair, S. Large Anomalous Nernst Effect across the Magneto-Structural Transition in a Bulk Ni-Co-Mn-Sn Full Heusler Alloy. *Appl. Phys. Lett.* **2018**, *113* (26), 262405.
- (27) De, A.; Singh, A. K.; Singh, S.; Nair, S. Temperature Dependence of the Anomalous Nernst Effect in Ni₂MnGa Shape Memory Alloy. *Phys. Rev. B* **2021**, *103* (2),

L020404.

- (28) Uchida, K.; Adachi, H.; Ota, T.; Nakayama, H.; Maekawa, S.; Saitoh, E. Observation of Longitudinal Spin-Seebeck Effect in Magnetic Insulators. *Appl. Phys. Lett.* **2010**, *97* (17), 172505.
- (29) Chanda, A.; Holzmann, C.; Schulz, N.; Seyd, J.; Albrecht, M.; Phan, M.-H.; Srikanth, H. Scaling of the Thermally Induced Sign Inversion of Longitudinal Spin Seebeck Effect in a Compensated Ferrimagnet: Role of Magnetic Anisotropy. *Adv. Funct. Mater.* **2022**, *32* (9), 2109170.
- (30) Kalappattil, V.; Das, R.; Phan, M.-H.; Srikanth, H. Roles of Bulk and Surface Magnetic Anisotropy on the Longitudinal Spin Seebeck Effect of Pt/YIG. *Sci. Rep.* **2017**, *7* (1), 13316.
- (31) Kehlberger, A.; Ritzmann, U.; Hinzke, D.; Guo, E.-J.; Cramer, J.; Jakob, G.; Onbasli, M. C.; Kim, D. H.; Ross, C. A.; Jungfleisch, M. B. Length Scale of the Spin Seebeck Effect. *Phys. Rev. Lett.* **2015**, *115* (9), 96602.
- (32) Uchida, K.; Kikkawa, T.; Miura, A.; Shiomi, J.; Saitoh, E. Quantitative Temperature Dependence of Longitudinal Spin Seebeck Effect at High Temperatures. *Phys. Rev. X* **2014**, *4* (4), 41023.
- (33) Guo, E.-J.; Cramer, J.; Kehlberger, A.; Ferguson, C. A.; MacLaren, D. A.; Jakob, G.; Kläui, M. Influence of Thickness and Interface on the Low-Temperature Enhancement of the Spin Seebeck Effect in YIG Films. *Phys. Rev. X* **2016**, *6* (3), 31012.
- (34) Ritzmann, U.; Hinzke, D.; Kehlberger, A.; Guo, E.-J.; Kläui, M.; Nowak, U. Magnetic Field Control of the Spin Seebeck Effect. *Phys. Rev. B* **2015**, *92* (17), 174411.
- (35) Geprägs, S.; Kehlberger, A.; Della Coletta, F.; Qiu, Z.; Guo, E.-J.; Schulz, T.; Mix, C.; Meyer, S.; Kamra, A.; Althammer, M. Origin of the Spin Seebeck Effect in Compensated Ferrimagnets. *Nat. Commun.* **2016**, *7* (1), 10452.

- (36) Chanda, A.; Holzmann, C.; Schulz, N.; Seyd, J.; Albrecht, M.; Phan, M.-H.; Srikanth, H. Scaling of the Thermally Induced Sign Inversion of Longitudinal Spin Seebeck Effect in a Compensated Ferrimagnet: Role of Magnetic Anisotropy. *Adv. Funct. Mater.* **2022**, *32*, 2109170.
- (37) Niizeki, T.; Kikkawa, T.; Uchida, K.; Oka, M.; Suzuki, K. Z.; Yanagihara, H.; Kita, E.; Saitoh, E. Observation of Longitudinal Spin-Seebeck Effect in Cobalt-Ferrite Epitaxial Thin Films. *AIP Adv.* **2015**, *5* (5), 53603.
- (38) Meier, D.; Kuschel, T.; Shen, L.; Gupta, A.; Kikkawa, T.; Uchida, K.; Saitoh, E.; Schmalhorst, J.-M.; Reiss, G. Thermally Driven Spin and Charge Currents in Thin NiFe₂O₄/Pt Films. *Phys. Rev. B* **2013**, *87* (5), 54421.
- (39) Xu, J.; He, J.; Zhou, J.-S.; Qu, D.; Huang, S.-Y.; Chien, C. L. Observation of Vector Spin Seebeck Effect in a Noncollinear Antiferromagnet. *Phys. Rev. Lett.* **2022**, *129* (11), 117202.
- (40) Holanda, J.; Santos, O. A.; Cunha, R. O.; Mendes, J. B. S.; Rodríguez-Suárez, R. L.; Azevedo, A.; Rezende, S. M. Longitudinal Spin Seebeck Effect in Permalloy Separated from the Anomalous Nernst Effect: Theory and Experiment. *Phys. Rev. B* **2017**, *95* (21), 214421.
- (41) Ramos, R.; Kikkawa, T.; Uchida, K.; Adachi, H.; Lucas, I.; Aguirre, M. H.; Algarabel, P.; Morellón, L.; Maekawa, S.; Saitoh, E. Observation of the Spin Seebeck Effect in Epitaxial Fe₃O₄ Thin Films. *Appl. Phys. Lett.* **2013**, *102* (7), 72413.
- (42) De, A.; Ghosh, A.; Mandal, R.; Ogale, S.; Nair, S. Temperature Dependence of the Spin Seebeck Effect in a Mixed Valent Manganite. *Phys. Rev. Lett.* **2020**, *124* (1), 17203.
- (43) Wu, B. W.; Luo, G. Y.; Lin, J. G.; Huang, S. Y. Longitudinal Spin Seebeck Effect in a Half-Metallic La_{0.7}Sr_{0.3}MnO₃ Film. *Phys. Rev. B* **2017**, *96* (6), 60402.

- (44) Jaworski, C. M.; Yang, J.; Mack, S.; Awschalom, D. D.; Heremans, J. P.; Myers, R. C. Observation of the Spin-Seebeck Effect in a Ferromagnetic Semiconductor. *Nat. Mater.* **2010**, *9* (11), 898–903.
- (45) He, B.; Sahin, C.; Boona, S. R.; Sales, B. C.; Pan, Y.; Felser, C.; Flatté, M. E.; Heremans, J. P. Large Magnon-Induced Anomalous Nernst Conductivity in Single-Crystal MnBi. *Joule* **2021**, *5* (11), 3057–3067.
- (46) Wang, X. L. Proposal for a New Class of Materials: Spin Gapless Semiconductors. *Phys. Rev. Lett.* **2008**, *100* (15), 156404.
- (47) Ouardi, S.; Fecher, G. H.; Felser, C.; Kübler, J. Realization of Spin Gapless Semiconductors: The Heusler Compound Mn_2CoAl . *Phys. Rev. Lett.* **2013**, *110* (10), 100401.
- (48) Alijani, V.; Winterlik, J.; Fecher, G. H.; Naghavi, S. S.; Felser, C. Quaternary Half-Metallic Heusler Ferromagnets for Spintronics Applications. *Phys. Rev. B* **2011**, *83* (18), 184428.
- (49) Bainsla, L.; Mallick, A. I.; Raja, M. M.; Nigam, A. K.; Varaprasad, B. S. D. C. S.; Takahashi, Y. K.; Alam, A.; Suresh, K. G.; Hono, K. Spin Gapless Semiconducting Behavior in Equiatomic Quaternary CoFeMnSi Heusler Alloy. *Phys. Rev. B* **2015**, *91* (10), 104408.
- (50) Bainsla, L.; Mallick, A. I.; Raja, M. M.; Coelho, A. A.; Nigam, A. K.; Johnson, D. D.; Alam, A.; Suresh, K. G. Origin of Spin Gapless Semiconductor Behavior in CoFeCrGa: Theory and Experiment. *Phys. Rev. B* **2015**, *92* (4), 45201.
- (51) Rani, D.; Bainsla, L.; Suresh, K. G.; Alam, A.; others. Spin-Gapless Semiconducting Nature of Co-Rich $Co_{1+x}Fe_{1-x}CrGa$. *Phys. Rev. B* **2019**, *99* (10), 104429.
- (52) Han, J.; Feng, Y.; Yao, K.; Gao, G. Y. Spin Transport Properties Based on Spin Gapless Semiconductor CoFeMnSi. *Appl. Phys. Lett.* **2017**, *111* (13).

- (53) Chandra, S.; Srikanth, H. Radio-Frequency Transverse Susceptibility as a Probe to Study Magnetic Systems. *Magn. Meas. Tech. Mater. Charact.* **2021**, 119–137.
- (54) Chanda, A.; Shoup, J. E.; Schulz, N.; Arena, D. A.; Srikanth, H. Tunable Competing Magnetic Anisotropies and Spin Reconfigurations in Ferrimagnetic Fe_{100-x}Gd_x Alloy Films. *Phys. Rev. B* **2021**, *104* (9), 94404.
- (55) Gartside, J. C.; Vanstone, A.; Dion, T.; Stenning, K. D.; Arroo, D. M.; Kurebayashi, H.; Branford, W. R. Reconfigurable Magnonic Mode-Hybridisation and Spectral Control in a Bicomponent Artificial Spin Ice. *Nat. Commun.* **2021**, *12* (1), 2488.
- (56) Chen, S. L.; Liu, W.; Zhang, Z. D.; Gunaratne, G. H. Magnetic Properties and Magnetic Domains of Nd-Fe-B Thin Films. *J. Appl. Phys.* **2008**, *103* (2), 23922.
- (57) Kazakova, O.; Puttock, R.; Barton, C.; Corte-León, H.; Jaafar, M.; Neu, V.; Asenjo, A. Frontiers of Magnetic Force Microscopy. *J. Appl. Phys.* **2019**, *125* (6), 60901.
- (58) Ge, W.; Sass, P. M.; Yan, J.; Lee, S. H.; Mao, Z.; Wu, W. Direct Evidence of Ferromagnetism in MnSb₂Te₄. *Phys. Rev. B* **2021**, *103* (13), 134403.
- (59) Ciubotariu, O.; Semisalova, A.; Lenz, K.; Albrecht, M. Strain-Induced Perpendicular Magnetic Anisotropy and Gilbert Damping of Tm₃Fe₅O₁₂ Thin Films. *Sci. Rep.* **2019**, *9* (1), 17474.
- (60) Rani, D.; Pandey, D. K.; Kimura, Y.; Umetsu, R. Y.; Chatterjee, R. Structural, Magnetic, and Transport Properties of Epitaxial Thin Films of Equiatomic Quaternary CoFeCrGa Heusler Alloy. *J. Appl. Phys.* **2022**, *132* (19), 193907.
- (61) Kushwaha, V. K.; Rani, J.; Tulapurkar, A.; Tomy, C. V. Possible Spin Gapless Semiconductor Type Behaviour in CoFeMnSi Epitaxial Thin Films. *Appl. Phys. Lett.* **2017**, *111* (15), 152407.
- (62) Kharel, P.; Zhang, W.; Skomski, R.; Valloppilly, S.; Huh, Y.; Fuglsby, R.; Gilbert, S.; Sellmyer, D. J. Magnetism, Electron Transport and Effect of Disorder in CoFeCrAl. *J.*

- Phys. D. Appl. Phys.* **2015**, *48* (24), 245002.
- (63) Srikanth, H.; Wiggins, J.; Rees, H. Radio-Frequency Impedance Measurements Using a Tunnel-Diode Oscillator Technique. *Rev. Sci. Instrum.* **1999**, *70* (7), 3097–3101.
- (64) Aharoni, A.; Frei, E. H.; Shtrikman, S.; Treves, D. The Reversible Susceptibility Tensor of the Stoner-Wohlfarth Model. *Bull. Res. Counc. Isr.* **1957**, *6*, 215–238.
- (65) Weiler, M.; Althammer, M.; Schreier, M.; Lotze, J.; Pernpeintner, M.; Meyer, S.; Huebl, H.; Gross, R.; Kamra, A.; Xiao, J.; others. Experimental Test of the Spin Mixing Interface Conductivity Concept. *Phys. Rev. Lett.* **2013**, *111* (17), 176601.
- (66) Xiao, J.; Bauer, G. E. W.; Uchida, K.; Saitoh, E.; Maekawa, S. Theory of Magnon-Driven Spin Seebeck Effect. *Phys. Rev. B* **2010**, *81* (21), 214418.
- (67) Rezende, S. M.; Rodríguez-Suárez, R. L.; Cunha, R. O.; Rodrigues, A. R.; Machado, F. L. A.; Guerra, G. A. F.; Ortiz, J. C. L.; Azevedo, A. Magnon Spin-Current Theory for the Longitudinal Spin-Seebeck Effect. *Phys. Rev. B* **2014**, *89* (1), 14416.
- (68) Arana, M.; Gamino, M.; Silva, E. F.; Barthem, V.; Givord, D.; Azevedo, A.; Rezende, S. M. Spin to Charge Current Conversion by the Inverse Spin Hall Effect in the Metallic Antiferromagnet Mn_2Au at Room Temperature. *Phys. Rev. B* **2018**, *98* (14), 144431.
- (69) Bougiatioti, P.; Klewe, C.; Meier, D.; Manos, O.; Kuschel, O.; Wollschläger, J.; Bouchenoire, L.; Brown, S. D.; Schmalhorst, J.-M.; Reiss, G. Quantitative Disentanglement of the Spin Seebeck, Proximity-Induced, and Ferromagnetic-Induced Anomalous Nernst Effect in Normal-Metal–Ferromagnet Bilayers. *Phys. Rev. Lett.* **2017**, *119* (22), 227205.
- (70) Kikkawa, T.; Uchida, K.; Shiomi, Y.; Qiu, Z.; Hou, D.; Tian, D.; Nakayama, H.; Jin, X.-F.; Saitoh, E. Longitudinal Spin Seebeck Effect Free from the Proximity Nernst Effect. *Phys. Rev. Lett.* **2013**, *110* (6), 67207.

- (71) Chanda, A.; DeTellem, D.; Hai Pham, Y. T.; Shoup, J. E.; Duong, A. T.; Das, R.; Cho, S.; Voronine, D. V.; Trinh, M. T.; Arena, D. A.; others. Spin Seebeck Effect in Iron Oxide Thin Films: Effects of Phase Transition, Phase Coexistence, and Surface Magnetism. *ACS Appl. Mater. Interfaces* **2022**, *14* (11), 13468–13479.
- (72) Jiménez-Cavero, P.; Lucas, I.; Bugallo, D.; López-Bueno, C.; Ramos, R.; Algarabel, P. A.; Ibarra, M. R.; Rivadulla, F.; Morellón, L. Quantification of the Interfacial and Bulk Contributions to the Longitudinal Spin Seebeck Effect. *Appl. Phys. Lett.* **2021**, *118* (9), 92404.
- (73) Ashworth, T.; Loomer, J. E.; Kreitman, M. M. Thermal Conductivity of Nylons and Apiezon Greases. In *Advances in Cryogenic Engineering*; Springer, 1973; pp 271–279.
- (74) Grimvall, G. *Thermophysical Properties of Materials*; Elsevier, 1999.
- (75) Marmion, S. R.; Ali, M.; McLaren, M.; Williams, D. A.; Hickey, B. J. Temperature Dependence of Spin Hall Magnetoresistance in Thin YIG/Pt Films. *Phys. Rev. B* **2014**, *89* (22), 220404.
- (76) Mott, N. F.; Jones, H.; Jones, H.; Jones, H. *The Theory of the Properties of Metals and Alloys*; Courier Dover Publications, 1958.
- (77) Reichlova, H.; Schlitz, R.; Beckert, S.; Swekis, P.; Markou, A.; Chen, Y.-C.; Kriegner, D.; Fabretti, S.; Hyeon Park, G.; Niemann, A.; others. Large Anomalous Nernst Effect in Thin Films of the Weyl Semimetal Co₂MnGa. *Appl. Phys. Lett.* **2018**, *113* (21), 212405.
- (78) Park, G.-H.; Reichlova, H.; Schlitz, R.; Lammel, M.; Markou, A.; Swekis, P.; Ritzinger, P.; Kriegner, D.; Noky, J.; Gayles, J.; others. Thickness Dependence of the Anomalous Nernst Effect and the Mott Relation of Weyl Semimetal Co₂MnGa Thin Films. *Phys. Rev. B* **2020**, *101* (6), 60406.
- (79) Asaba, T.; Ivanov, V.; Thomas, S. M.; Savrasov, S. Y.; Thompson, J. D.; Bauer, E. D.;

- Ronning, F. Colossal Anomalous Nernst Effect in a Correlated Noncentrosymmetric Kagome Ferromagnet. *Sci. Adv.* **2021**, 7 (13), eabf1467.
- (80) Li, X.; Xu, L.; Ding, L.; Wang, J.; Shen, M.; Lu, X.; Zhu, Z.; Behnia, K. Anomalous Nernst and Righi-Leduc Effects in Mn₃Sn: Berry Curvature and Entropy Flow. *Phys. Rev. Lett.* **2017**, 119 (5), 56601.
- (81) Jin, H.; Boona, S. R.; Yang, Z.; Myers, R. C.; Heremans, J. P. Effect of the Magnon Dispersion on the Longitudinal Spin Seebeck Effect in Yttrium Iron Garnets. *Phys. Rev. B* **2015**, 92 (5), 54436.
- (82) Ritzmann, U.; Hinzke, D.; Nowak, U. Propagation of Thermally Induced Magnonic Spin Currents. *Phys. Rev. B* **2014**, 89 (2), 24409.
- (83) Dürrenfeld, P.; Gerhard, F.; Chico, J.; Dumas, R. K.; Ranjbar, M.; Bergman, A.; Bergqvist, L.; Delin, A.; Gould, C.; Molenkamp, L. W.; others. Tunable Damping, Saturation Magnetization, and Exchange Stiffness of Half-Heusler NiMnSb Thin Films. *Phys. Rev. B* **2015**, 92 (21), 214424.
- (84) Nembach, H. T.; Silva, T. J.; Shaw, J. M.; Schneider, M. L.; Carey, M. J.; Maat, S.; Childress, J. R. Perpendicular Ferromagnetic Resonance Measurements of Damping and Landé g -Factor in Sputtered (Co₂Mn)_{1-x}Ge_x Thin Films. *Phys. Rev. B* **2011**, 84 (5), 54424.
- (85) Mosendz, O.; Pearson, J. E.; Fradin, F. Y.; Bauer, G. E. W.; Bader, S. D.; Hoffmann, A. Quantifying Spin Hall Angles from Spin Pumping: Experiments and Theory. *Phys. Rev. Lett.* **2010**, 104 (4), 46601.
- (86) Jermain, C. L.; Aradhya, S. V.; Reynolds, N. D.; Buhrman, R. A.; Brangham, J. T.; Page, M. R.; Hammel, P. C.; Yang, F. Y.; Ralph, D. C. Increased Low-Temperature Damping in Yttrium Iron Garnet Thin Films. *Phys. Rev. B* **2017**, 95 (17), 174411.
- (87) Seiden, P. E. Ferrimagnetic Resonance Relaxation in Rare-Earth Iron Garnets. *Phys.*

- Rev.* **1964**, *133* (3A), A728.
- (88) Vilela, G. L. S.; Abrao, J. E.; Santos, E.; Yao, Y.; Mendes, J. B. S.; Rodríguez-Suárez, R. L.; Rezende, S. M.; Han, W.; Azevedo, A.; Moodera, J. S. Magnon-Mediated Spin Currents in Tm₃Fe₅O₁₂/Pt with Perpendicular Magnetic Anisotropy. *Appl. Phys. Lett.* **2020**, *117* (12), 122412.
- (89) Guo, S.; McCullian, B.; Hammel, P. C.; Yang, F. Low Damping at Few-K Temperatures in Y₃Fe₅O₁₂ Epitaxial Films Isolated from Gd₃Ga₅O₁₂ Substrate Using a Diamagnetic Y₃Sc₂.₅Al₂.₅O₁₂ Spacer. *J. Magn. Magn. Mater.* **2022**, *562*, 169795.
- (90) Crossley, S.; Quindeau, A.; Swartz, A. G.; Rosenberg, E. R.; Beran, L.; Avci, C. O.; Hikita, Y.; Ross, C. A.; Hwang, H. Y. Ferromagnetic Resonance of Perpendicularly Magnetized Tm₃Fe₅O₁₂/Pt Heterostructures. *Appl. Phys. Lett.* **2019**, *115* (17), 172402.
- (91) Haertinger, M.; Back, C. H.; Lotze, J.; Weiler, M.; Geprägs, S.; Huebl, H.; Gönnerwein, S. T. B.; Woltersdorf, G. Spin Pumping in YIG/Pt Bilayers as a Function of Layer Thickness. *Phys. Rev. B* **2015**, *92* (5), 54437.
- (92) Uchida, K.; Qiu, Z.; Kikkawa, T.; Iguchi, R.; Saitoh, E. Spin Hall Magnetoresistance at High Temperatures. *Appl. Phys. Lett.* **2015**, *106* (5), 52405.

Supplementary Information

Large thermo-spin effects in Heusler alloy based spin-gapless semiconductor thin films

Amit Chanda^{1*}, Deepika Rani², Derick DeTelle¹, Noha Alzahrani¹, Dario A. Arena¹, Sarath
Witanachchi¹, Ratnamala Chatterjee², Manh-Huong Phan¹ and Hariharan Srikanth^{1*}

¹ Department of Physics, University of South Florida, Tampa FL 33620

² Physics Department, Indian Institute of Technology Delhi, New Delhi - 110016

**Corresponding authors: achanda@usf.edu; sharihar@usf.edu*

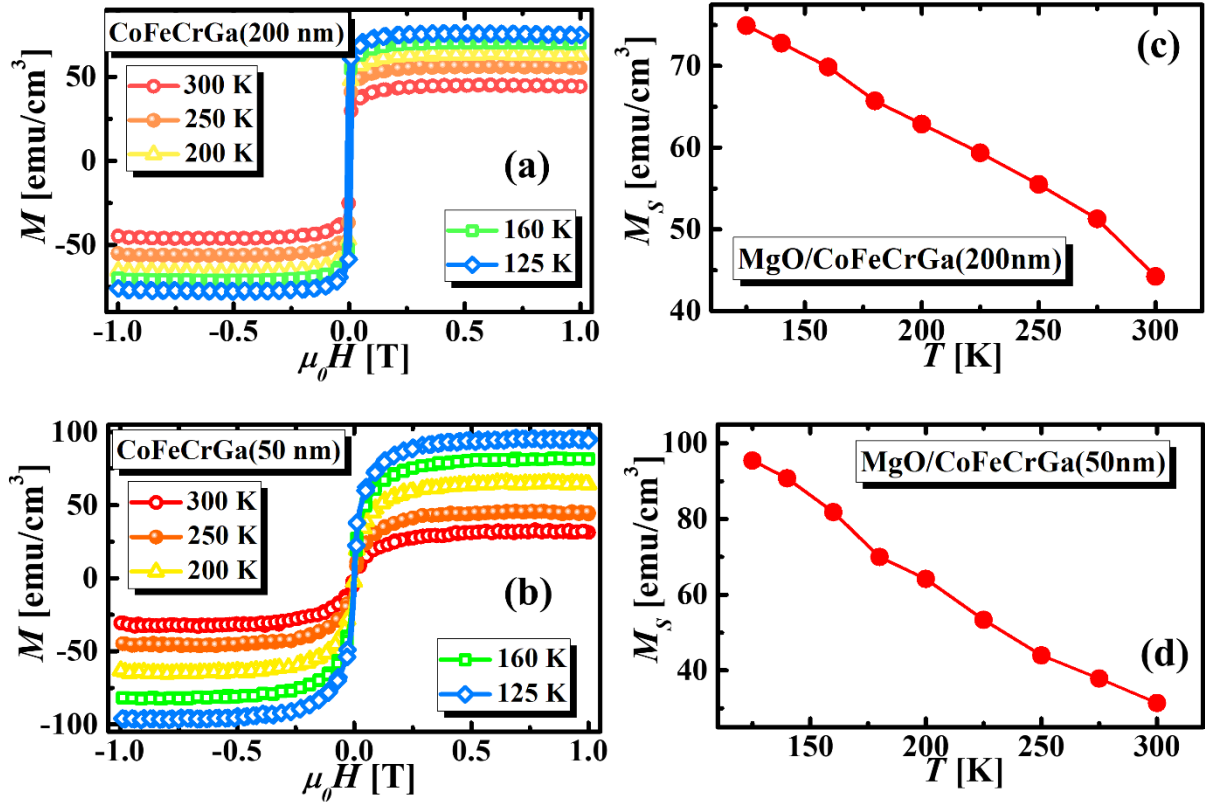


Figure S1. (a) and (b) Magnetic field dependence of magnetization, $M(H)$ of our MgO/CoFeCrGa(200nm) and MgO/CoFeCrGa(50nm)/Pt films, respectively measured at selected temperatures in the range: $125 \text{ K} \leq T \leq 300 \text{ K}$ in presence of an in-plane sweeping magnetic field, (c) and (d) temperature dependence of the saturation magnetization, M_S for the same films, respectively.

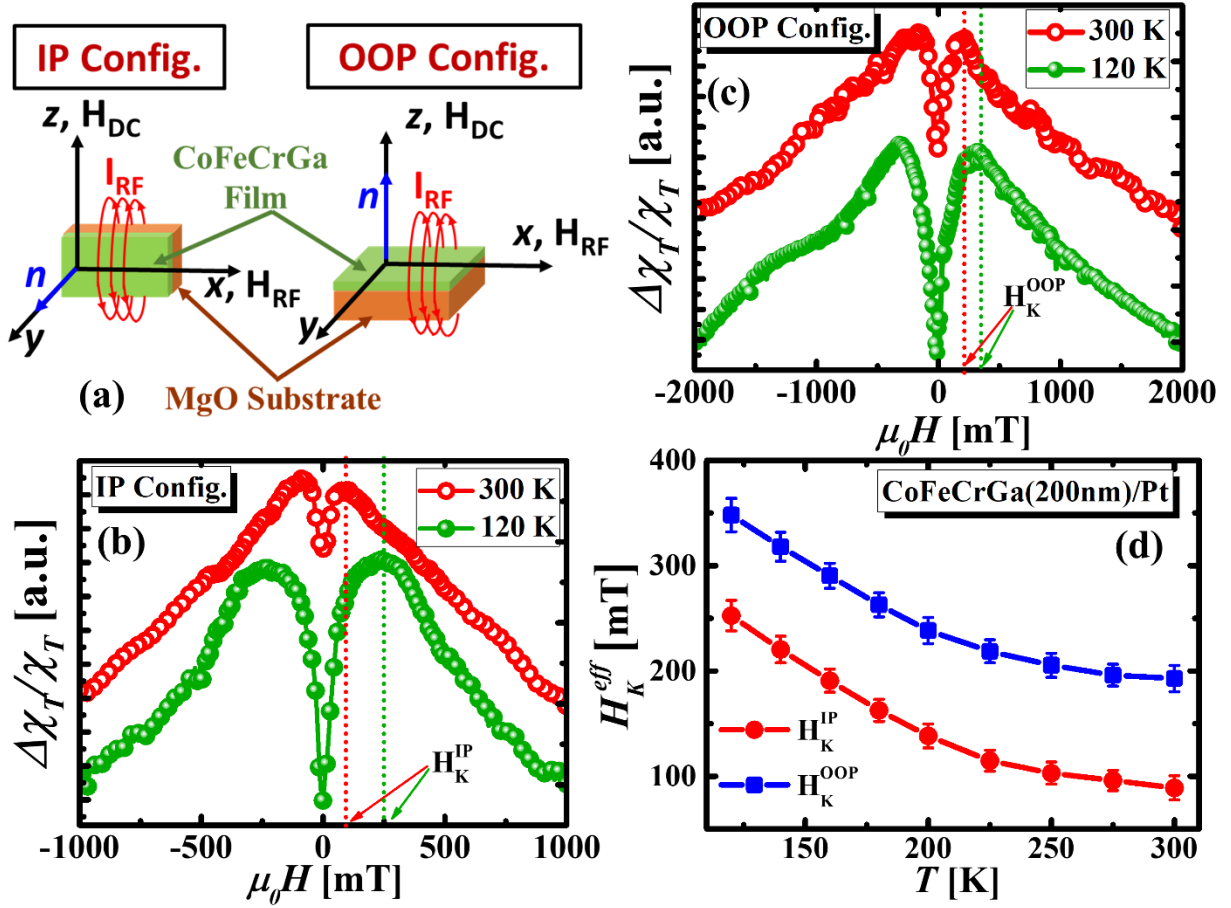


Figure S2. (a) Schematic illustration of the transverse susceptibility (TS) measurements. The bipolar field scans ($+H_{DC}^{max} \rightarrow -H_{DC}^{max} \rightarrow +H_{DC}^{max}$) of the field dependence of TS, $\frac{\Delta\chi_T}{\chi_T}(H_{DC})$ for the MgO/CoFeCrGa(200nm)/Pt(5nm) film measured at $T = 300$ K and 20 K for the (b) IP (H_{DC} is parallel to the film surface) and (c) OOP (H_{DC} is perpendicular to the film surface) configurations. (d) Temperature variations of the effective anisotropy fields: H_K^{IP} and H_K^{OOP} for the MgO/CoFeCrGa(200nm)/Pt film.

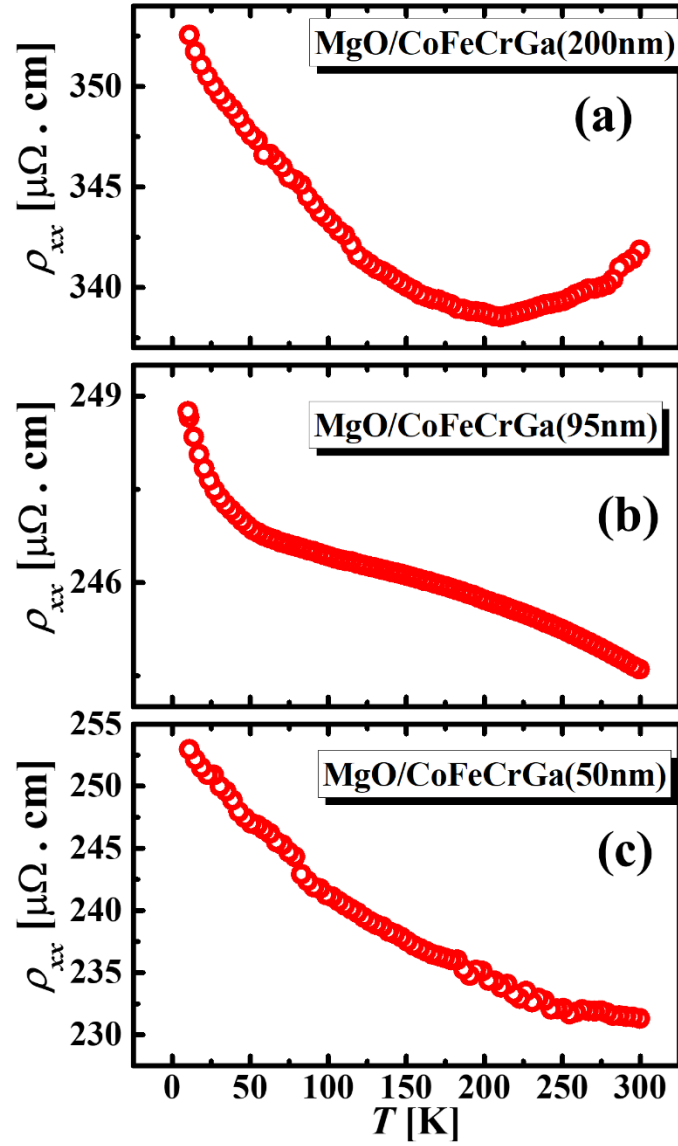


Figure S3. Temperature dependence of longitudinal resistivity, $\rho_{xx}(T)$ for the (a) MgO/CoFeCrGa(200nm), (b) MgO/CoFeCrGa(95nm) and (c) MgO/CoFeCrGa(200nm) films, respectively in the temperature range: $10 \text{ K} \leq T \leq 300 \text{ K}$.

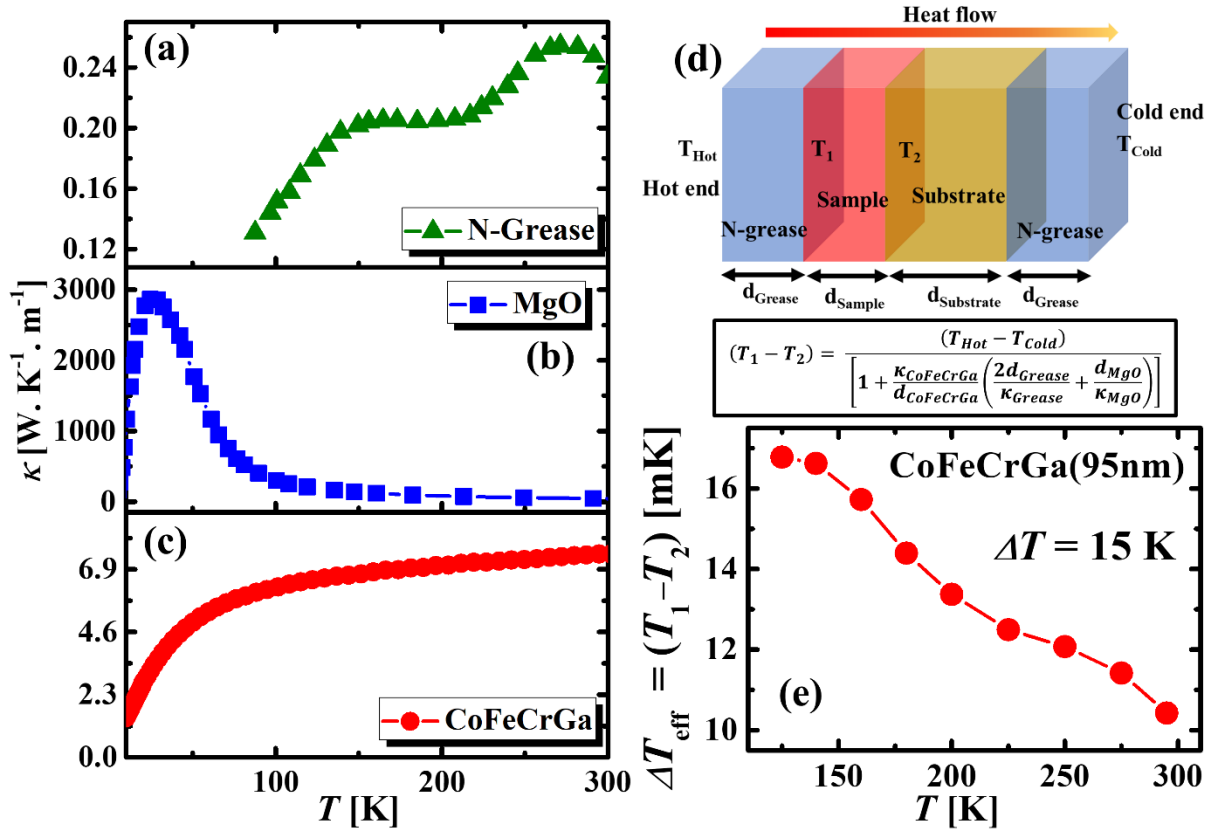


Figure S4. Temperature variations of thermal conductivity of (a) Apiezon N-grease,¹ (b) MgO crystal² and (c) bulk CoFeCrGa (measured) using the thermal transport option (TTO) of the PPMS. (d) Schematic illustration of the heat flow through N-grease/MgO substrate/CoFeCrGa film/N-grease considering the 4-slab model. (e) The temperature variation of the effective temperature difference across the MgO/CoFeCrGa(95nm) film estimated from the expression,³

$$\Delta T_{eff} = \Delta T_{CoFeCrGa} = \frac{\Delta T}{\left[1 + \frac{\kappa_{CoFeCrGa}}{t_{CoFeCrGa}} \left(\frac{2t_{N-Grease}}{\kappa_{N-Grease}} + \frac{t_{MgO}}{\kappa_{MgO}} \right) \right]}$$

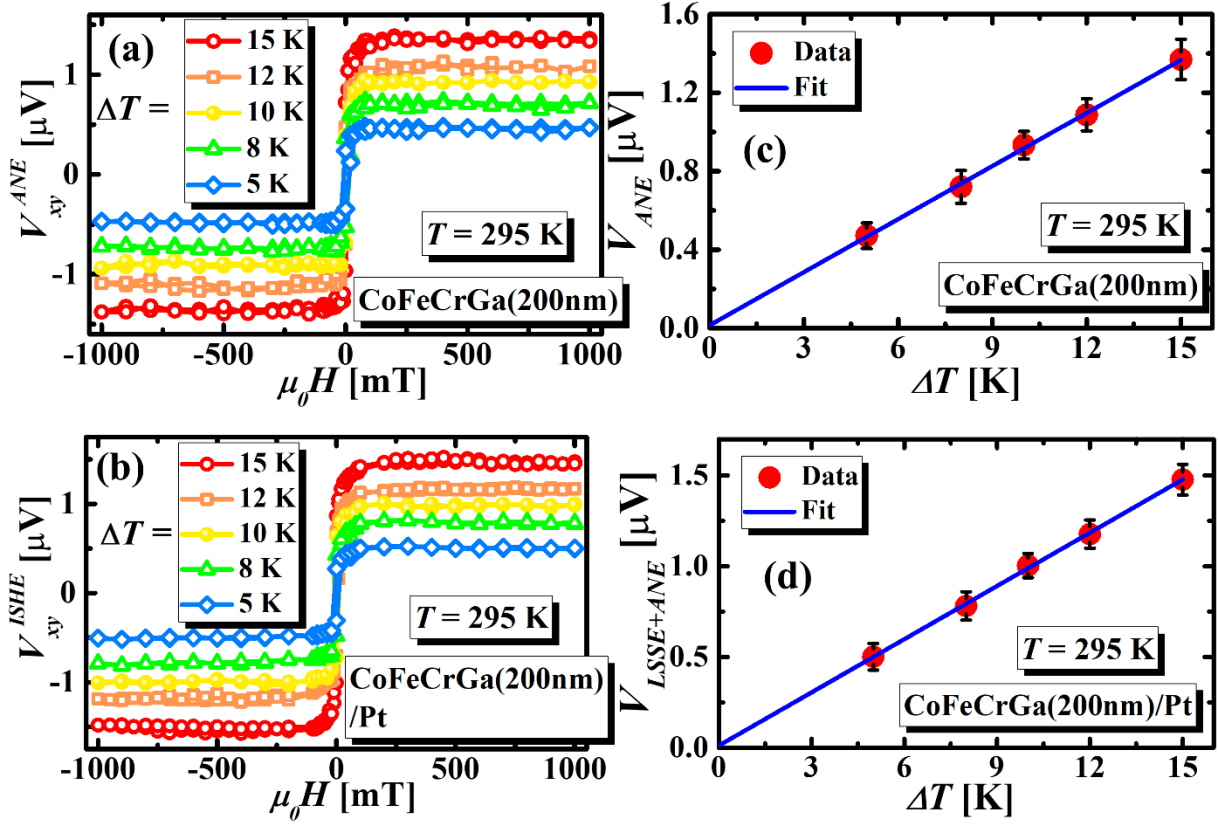


Figure S5. (a) and (b) The magnetic field dependence of the ANE voltage, $V_{ANE}(H)$ and ISHE-induced in-plane voltage, $V_{ISHE}(H)$ measured on the MgO/CoFeCrGa(200nm) and MgO/CoFeCrGa(200nm)/Pt films, respectively for different values of the temperature difference between the hot (T_{hot}) and cold (T_{cold}) copper blocks, $\Delta T = (T_{hot} - T_{cold})$ in the range: $+5 \text{ K} \leq \Delta T \leq +18 \text{ K}$ at a fixed average sample temperature $T = \frac{T_{hot} + T_{cold}}{2} = 295 \text{ K}$. (c) and (d) The ΔT dependence of the background-corrected ANE voltage, $V_{ANE}(\Delta T) = \left[\frac{V_{ANE}(+\mu_0 H_{max}, \Delta T) - V_{ANE}(-\mu_0 H_{max}, \Delta T)}{2} \right]$ and the background-corrected (ANE+LSSE) voltage, $V_{ANE+LSSE}(\Delta T) = \left[\frac{V_{ISHE}(+\mu_0 H_{max}, \Delta T) - V_{ISHE}(-\mu_0 H_{max}, \Delta T)}{2} \right]$, respectively.

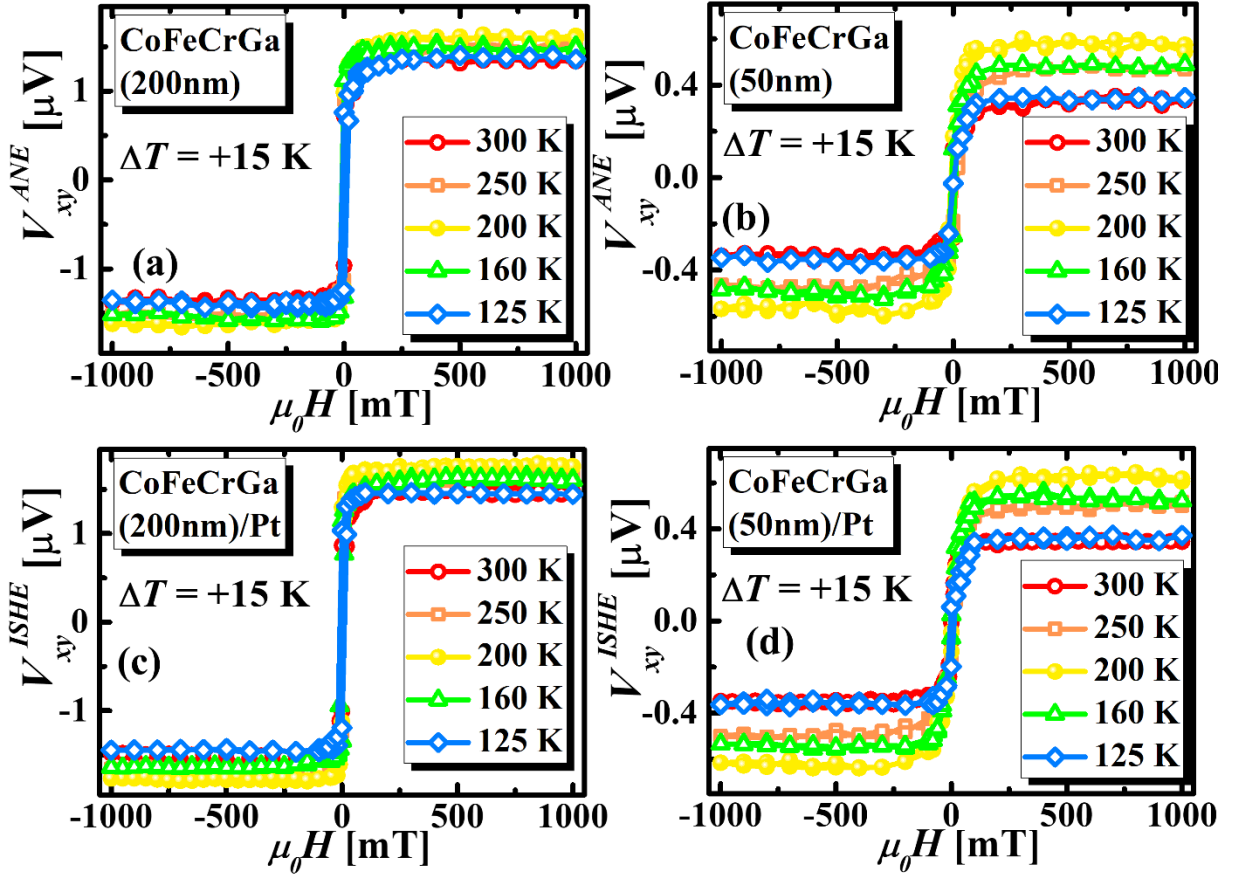


Figure S6. (a) and (b) $V_{ANE}(H)$ hysteresis loops measured at selected average sample temperatures in the temperature range: $125 \text{ K} \leq \Delta T \leq 295 \text{ K}$ for a fixed value of $\Delta T = +15$ K on the MgO/CoFeCrGa(200nm) and MgO/CoFeCrGa(500nm) films, respectively. (c) and (d) $V_{ISHE}(H)$ hysteresis loops measured at selected average sample temperatures in the temperature range: $125 \text{ K} \leq \Delta T \leq 295 \text{ K}$ for a fixed value of $\Delta T = +15$ K on the MgO/CoFeCrGa(200nm)/Pt and MgO/CoFeCrGa(50nm)/Pt films, respectively.

References

- (1) Ashworth, T.; Loomer, J. E.; Kreitman, M. M. Thermal Conductivity of Nylons and Apiezon Greases. In *Advances in Cryogenic Engineering*; Springer, 1973; pp 271–279.
- (2) Grimvall, G. *Thermophysical Properties of Materials*; Elsevier, 1999.
- (3) De, A.; Ghosh, A.; Mandal, R.; Ogale, S.; Nair, S. Temperature Dependence of the Spin Seebeck Effect in a Mixed Valent Manganite. *Phys. Rev. Lett.* **2020**, *124* (1), 17203.